UNIVERSITY OF TWENTE.
Faculty of Electrical Engineering,
Mathematics & Conputer Science

Exploring Nonlinear Dynamics
in Al_2O_3 Integrated Photonic Devices

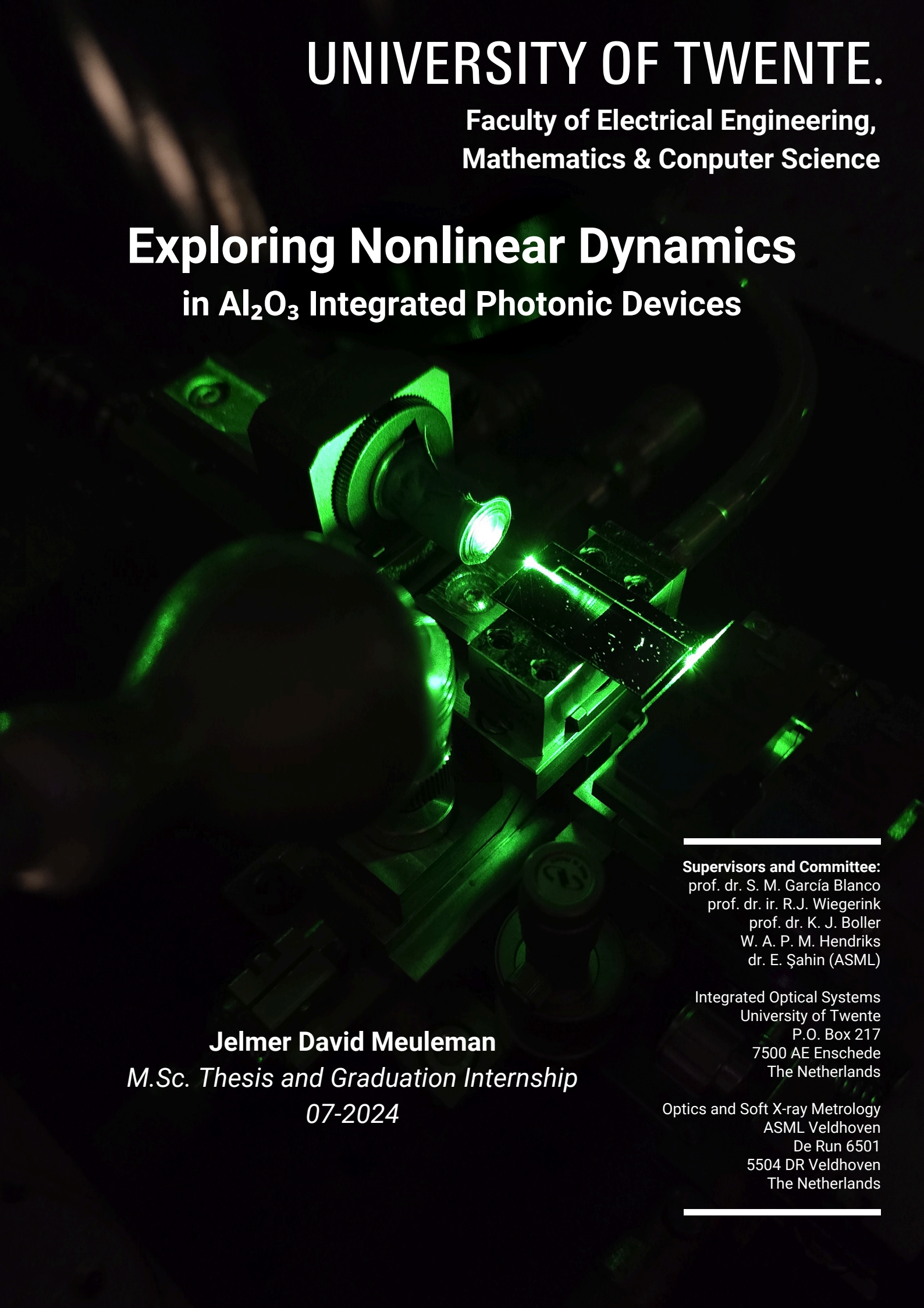

Jelmer David Meuleman

M.Sc. Thesis and Graduation Internship
07-2024

Supervisors and Committee:
prof. dr. S. M. García Blanco
prof. dr. ir. R.J. Wiegerink
prof. dr. K. J. Boller
W. A. P. M. Hendriks
dr. E. Şahin (ASML)

Integrated Optical Systems
University of Twente
P.O. Box 217
7500 AE Enschede
The Netherlands

Optics and Soft X-ray Metrology
ASML Veldhoven
De Run 6501
5504 DR Veldhoven
The Netherlands

Preface

You are reading what should be the culmination of many years of growing at the University of Twente. Both my BSc in Electrical Engineering and my MSc in Integrated Optical Systems, have shown me that magic ís real, you just have to look very closely at the things you find normal.

This thesis project, which was intended to be small, kept on growing under the enthusiasm of everyone involved. Likewise, it kept on growing in terms of people and stakeholders, from investors at ASML to retired professors, from old friends to new.

All this means I have a huge list of people to thank, and I am truly grateful for all the support and insights I've been given over these 7 months. In particular, I want to thank Ward (IOS) and Ezgi (AMSL), my daily supervisors, who made time in their busy schedules. Ward, I want to thank you not just for this project, but for the past 2.5 years in all. I've learned so much, I consider you a friend, and I hope that this isn't the last we'll be seeing of each other! Ezgi, your interest and willingness to help, both in scientific matters and personal ones, has been a great motivation. I don't think I would have made it half-way without you!

I would also like to thank both Lisi (LPNO) and Yvan (NLNP), who allowed me to work with their valuable equipment and offered me their valuable time for help. Thank you for the endless amount of system iterations!

And of course, a big thanks to the rest of my committee. Professors Sonia (IOS) and Klaus (LPNO). Your trust and freedom have made it possible to pursue this project to the end. You two have taught me how to navigate the dangerous waters of academic communication/organization, something which I'm sure will be essential in the years to come. I would also like to thank Professor Remco (IDS) who stepped in to fill the final position on the committee at the last minute.

Then last, but certainly not least, I would like to thank my friends. Their friendship, warmth, and laughs have made sure I kept sane these months (fire pictures not included ☺). And most of all, I want to thank Femke, my love, my life, who has supported me tremendously all this time. After 8 years my love has only grown and I can't wait to see what we will do in this next phase of life! To infinity and beyond..

Jelmer David Meuleman
Juli 2024, Enschede

Contents

Chapter 1

Introduction

1.1 Motivation

Integrated photonic circuits (PICs) have become crucial components of many technological applications, spanning: telecommunications, (medical) sensors, environmental sensors, laser technology, quantum computing, and many more [1]–[8]. Supercontinuum generation (SCG) is a key process used for several of these applications. This is the nonlinear broadening of an input spectrum into an often dramatically wider spectrum. Also called white-light generation, supercontinuum generation finds its use in applications like spectroscopy, wavelength-division multiplexing, and metrology [9], [10].

While SCG in optical fibers has been demonstrated since the 1970s [11], SCG in PICs has been getting more traction as fabrication technology advances. The increased performance of the integrated platforms has facilitated many benefits like easy integration with other optical systems on chip, and devices becoming more compact. The latter of which has significance, as the denser the confinement of the light, the higher the power density can be as well, which allows for more efficient nonlinear processes like that of SCG. Another great benefit is that PICs allow for more freedom in dispersion engineering by varying the geometry of waveguides, which unlocks new dimensions for optimization.

While there have been great advancements in SCG technology in PIC platforms, such as Si3N4 [12], there is one major drawback that exists in many platforms. The transparency windows are often limited to above UV wavelengths, placing a hard barrier on the high-energy end of SCG [13]. For this reason, Al_2O_3 is identified as a material of interest for SCG expending into the blue and UV, as it has a very broad transparency window ranging from 170 nm UV to the mid-IR [14]. It can also readily be manufactured today and exhibits low propagation losses of the order of < 0.1

dB/cm in the C-band. Although Al_2O_3 is known to have a relatively low nonlinear index around $2 \cdot 10^{-20}$ to $3 \cdot 10^{-20}$ m^2/W in *bulk* materials [15], with the exact nonlinear index in polycrystalline waveguides unknown, the large transparency window should give it an edge over more conventional materials used in nonlinear optics on chip.

To further explore the possibilities for SCG in Al_2O_3 PICs, this thesis aims to bridge the gap between theoretical simulations and practical implementations by measuring fabricated Al_2O_3 waveguides with high-power pulses of light to obtain the parameters of interest for nonlinear engineering. Aiming to gather valuable information about real-world SCG, as well as information on physical limits such as the damage threshold of the platform. Moreover, as measurements of the nonlinear refractive index of polycrystalline Al_2O_3 waveguides have to the best of our knowledge not been published, this research will include measurements aimed at acquiring a dependable value. Information like this is very valuable for future research and the development of nonlinear systems and should aid in pushing the Al_2O_3 forward.

1.2 Research objectives

This thesis focuses on the feasibility of broadband supercontinuum generation in Al_2O_3 waveguides. The main objective is to gather more information about the behaviour of Al_2O_3 in the nonlinear optical regime through measurements. As this project is divided into two parts, there will be two research questions, the first being:

Is it possible to demonstrate supercontinuum generation in Al_2O_3 based integrated waveguides?

Which will include the following sub-question:
What is the damage threshold of Al_2O_3 for ultra-fast pulsed lasers?

To better understand, model, and design for nonlinear applications, it is also of great importance to have more accurate knowledge of the material parameters at play. For this reason, the second research question will be:

What is the nonlinear refractive index of polycrystalline Al_2O_3 based integrated waveguides?

Which will include the following sub-question:
What is the damage threshold of Al_2O_3 for continuous-wave lasers?

1.3 Report organization

In this thesis, the chapters are organised by experiment.

Chapter 2 will describe the work done on supercontinuum generation. It starts with a general introduction to the theory and underlying principles of supercontinuum generation. This is followed by an explanation of the design choices and procedures for the PICs. After this, simulations are shown of the theoretical performance for a high-power pulsed laser at the design wavelength of 1064 nm. Finally, lab results of measurements with a 1550 nm high-power pulsed laser are shown and further discussed.

Chapter 3 will describe the work done on the determination of the nonlinear refractive index. It highlights the measurements regarding characterization of the micro-ring resonator and the measurements of four-wave mixing used for the analysis, closing by presenting the nonlinear index of Al_2O_3.

Finally, an overall conclusion is given with outlooks for future research.

Chapter 2

Supercontinuum Generation chips

2.1 Introduction

Supercontinuum generation (SCG) is the process of transforming laser light of a narrow bandwidth, into a broad continuous spectrum [16]. It is a process that works through a collection of nonlinear effects that together can drastically change the spectral bandwidth of the input to the system.

SCG is usually achieved by propagating high-power light pulses through a nonlinear material, which can be waveguides, as used here, fibers or bulk materials. SCG can be classified in two types: normal dispersion SCG and anomalous dispersion SCG [17]. The group velocity dispersion (GVD) of the material determines which type occurs (this is covered more in Section 2.2). To get a feeling for the differences, Figure 2.1 shows examples of both. Notice the smooth spectral transition of the normal dispersion SCG compared to the dramatic and more chaotic broadening of the anomalous SCG. It is this dramatic broadening that we want to leverage with this research, working towards SCG extending into the UV. Thus making anomalous dispersion SCG the central objective of our design choices.

This chapter will explore the feasibility of using Al_2O_3 for supercontinuum generation, with the goal of working towards SCG that extends into the UV. The primary focus is on the design and theoretical capabilities of PICs made in the Al_2O_3 platform at the University of Twente spin-off ALUVIA [18]. Also covered are high power bands in the spectrum called dispersive waves, whose wavelength can be tuned with dispersion engineering. Finally, the results of experimental measurements are highlighted to demonstrate nonlinear processes in Al_2O_3.

Sections 2.2.1 and 2.2.2 will cover a general explanation of some fundamental concepts and processes that are involved in SCG. Including the optical Kerr effect

and $\chi^{(3)}$ nonlinearities. Section 2.3 will cover the design choices made for the fabricated PICs and fabrication. Section 2.4 will cover the methods and will present experimental results, and finally Section 2.5 will conclude the chapter with a general conclusion and discussion.

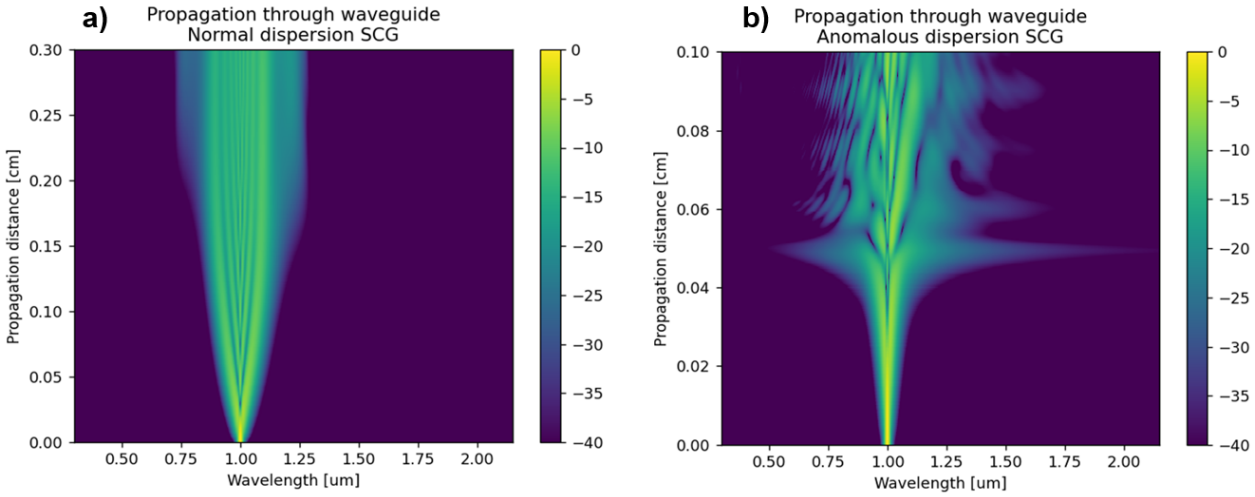

Figure 2.1: Examples of supercontinuum generation with a) normal dispersion, b) anomalous dispersion. Image taken from internship report, see Appendix A

2.2 Theoretical groundwork

2.2.1 Fundamental Concepts

Optical Kerr effect

The Optical Kerr effect is a fundamental concept in nonlinear optics. It governs the change in refractive index of a material based on the intensity of light passing through it [19], [20]. This process is at the base of many of the processes in supercontinuum generation.

In general, the dependence of the electric dipole moment per unit volume $\mathbf{P}(t)$ can be described by a power series [21]:

$$\mathbf{P}(t) = \epsilon_0(\chi^{(1)}\mathbf{E}(t) + \chi^{(2)}\mathbf{E}^2(t) + \chi^{(3)}\mathbf{E}^3(t) + ...) \tag{2.1}$$

Where $\mathbf{E}(t)$ is the electric field, ϵ_0 is the permittivity of free space and $\chi^{(i)}$ is the i-th order susceptibility of the material. In the linear photonics regime, the susceptibilities of the response of the material to the E-field is limited to $\chi^{(1)}$, with any higher susceptibilities being negligible, leading to a polarization that is directly proportional to the electric field:

$$\mathbf{P}_{\text{linear}}(t) = \epsilon_0\chi^{(1)}\mathbf{E}(t) \tag{2.2}$$

In the nonlinear photonics regime however, this approximation is insufficient. When the intensity of the electric field is high, or when the medium material is strongly nonlinear, the higher order susceptibilities terms can become significant. Note that even-order susceptibilities are often still negligible as many materials, including Al_2O_3, display inversion symmetry. In material with inversion symmetry the physical properties of a material, including the response to electric field, must remain the same when all spatial coordinates are inverted. For even-ordered powers, there is no cumulative sign change when all electric field are inverted ($-1^{\text{even}} = 1$) meaning that the susceptibility of the material in both positive and negative direction must be equal, i.e. $\chi^{(\text{even})} = -\chi^{(\text{even})}$, which can only be true is the susceptibility is zer0 [21].

The Optical Kerr effect arises from the third-order susceptibility $\chi^{(3)}$, which leads to a nonlinear polarization component:

$$\mathbf{P}_{\text{nonlinear}}(t) = \epsilon_0\chi^{(3)}\mathbf{E}^3(t) \tag{2.3}$$

This nonlinear component results in an intensity I dependent change in the re-

fractive index of the medium, and this specifically is what the Kerr effect refers to, following the equation below [19], [20]:

$$n = n_0 + n_2 I, \tag{2.4}$$

where n_0 is the linear refractive index and n_2 is the nonlinear refractive index due to the $\chi^{(3)}$ susceptibility.

Group velocity dispersion

Another fundamental concept in nonlinear optics is dispersion. Dispersion describes how different wavelengths of light can travel at different speeds through a medium. This can have a significant effect on the propagation of light pulses through a medium.

Group velocity dispersion, as the name implies, is the dependence of the group velocity on the wavelength of the light. The group velocity itself is the speed at which the envelope of a pulse of light travels through a medium [22]. GVD can be responsible for dispersive broadening or compression of pulses, something which is essential in our supercontinuum generation. Mathematically, the GVD (β_2) can be describes as:

$$\beta_2 = \frac{\partial^2 \beta(\omega)}{\partial \omega^2} \tag{2.5}$$

where β is the wavenumber or phase constant in a waveguide, and ω is the angular frequency of the light. The sign of β_2 indicates the dispersion regime. A positive β_2 denotes the *normal* dispersion regime, while a negative β_2 denotes the *anomalous* dispersion regime[1].

For normal group velocity dispersion (so $\beta_2 > 0$) the short wavelength components of the pulse travel slower than the long wavelength components. This is the most common situation and leads to temporal broadening (unless the initial pulse is downchirped [23]). For anomalous group velocity dispersion ($\beta_2 > 0$) the shorter wavelength components of the pulse travel faster. This can be used to counteract the effects of self-phase modulation (SPM) in a medium, which is useful as this allows the creating of solitons, i.e. wave packets that can keep their shape for long distances [24], and is discussed more in Section 2.2.3.

Although the intrinsic group velocity dispersion of a material is constant, the total GVD can still be influenced by the geometry of a waveguide or fiber. Dispersion en-

[1] In fiber optics, group velocity dispersion is often expressed as $D_\lambda = -\frac{2\pi c}{\lambda^2} \cdot \beta_2$. In this definition, the *anomalous* dispersion region is indicated by a *positive* GVD.

gineering relates to the manipulation of the GVD through both material choice and geometry, and is used to achieve desired dispersion characteristics [25]. Something that can also be levered to optimise systems for supercontinuum generation.

2.2.2 Mechanisms of Supercontinuum Generation

Someone once told me that *"supercontinuum generation is like a black box, where all kinds of nonlinear processes are mixed and no one quite exactly knows what happens inside"* (K.J. Boller, private communication, Feb., 2024). But even so, we can look at the different nonlinear processes dependent on the $\chi^{(3)}$ susceptibility as SCG is an interplay of many of these effects [16], [26]. Figure 2.2 shows a visual overview of a number of nonlinear effects governed by $\chi^{(3)}$, split into different categories. The rest of this section will highlight these processes and give a short recap of each.

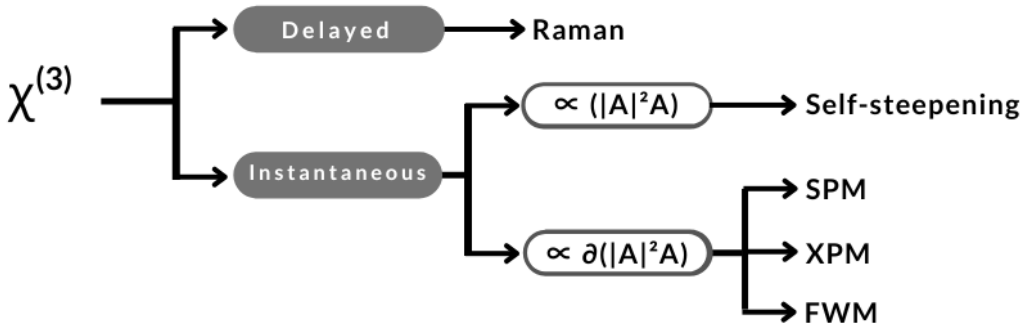

Figure 2.2: A number of $\chi^{(3)}$ based nonlinear processes

Raman scattering

Raman scattering is an inelastic scatting process where energy can be transferred from lower wavelength to higher wavelength (or in reverse for anti-Stokes Raman scattering) [21]. It is caused by an interaction between the light and the molecular lattice of the medium, and as the movement of the vibrational states of the material is very slow to that compared of electrons, it is placed as the only 'delayed' effect in Figure 2.2.

The most prevalent form is Stokes-Raman scatting which occurs when a photon excites the medium to a higher (virtual) energy state, after which the medium relaxes to a vibrational state with higher energy still than the original state. This energy transfer to the medium leaves the photon with less energy and thus a lower wavelength [ref], see also Figure 2.3a.

Anti-Stokes-Raman is the opposite. When the medium is excited while already being in a higher energy vibrational state, it can relax down to a state with lower energy after decay, leaving the photon with more energy and thus a higher wavelength. Here the energy transfer is from the medium to the photon, see Figure 2.3b.

Typically, Stokes-Raman scatting is much more common than its opposite Anti-Stokes-Raman scattering [27]. For the supercontinuum spectrum this means that on average Stokes-Raman scatting is prevalent, resulting in a red-shift of the spectrum. Raman scatting can also effectively act on soliton pulses, where the process is also called soliton self-frequency shift [27].

Figure 2.3: A schematic overview of a) Stokes-Raman and; b) Anti-Stokes-Raman scatting. Notice the difference in energy that is being lost or gained to the vibrational modes in the medium.

Self-steepening

Self-steepening is a nonlinear effect that refers to the temporal distortion of an optical pulse. More specifically it causes the steepening of the trailing edge of the pulse, due to a dependency of the group index n_g of the pulse on the intensity of the light, where n_g increases for higher intensity [16]. The effect can be explain by a combination of the Kerr effect and the contribution of the time-derivative of the intensity to the nonlinear phase, which accumulates towards the trailing edge of the pulse. This time-derivative dependency on the intensity or envelope of the light is why Self-steepening is placed in a separate section in Figure 2.2.

Due to self-steepening, a symmetric pulse gets stretched out in the temporal domain, as the leading edge moves faster (lower n_g) compared to the higher intensity center (higher n_g). The slowed energy accumulates at the trailing end, giving it a steeper slope, see Figure 2.4.

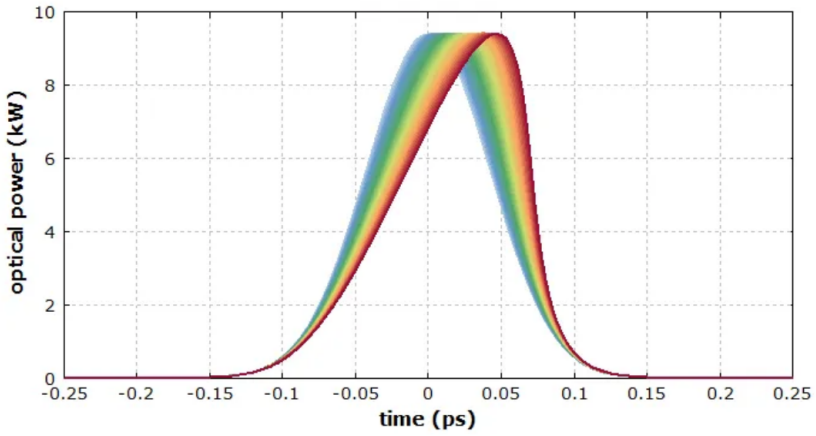

Figure 2.4: The effect of self-steepening on a Gaussian pulse. Notice the steeper slope at the right-hand (trailing) side of the pulse. Image source: [28]

Self-steepening typically leads to a blue-shift in the spectrum. The asymmetry leads to a higher power density at the trailing (blue) edge. This leads to faster, i.e. more broadband, modulation due to the Kerr effect, while the opposite is true on the leading (red) edge. Self-steepening has also been shown to decrease the self-frequency shift induced by the Raman effect [29].

Self-Phase Modulation (SPM)

Self-Phase Modulation (SPM) is a nonlinear effect that plays a significant role in SCG, both in normal dispersion and in anomalous dispersion [21], [30]. The effect itself describes how the phase of a pulse is modulated by its own intensity, which arises directly from the Kerr effect (see Equation 2.4). It is typically written as:

$$\phi_{\text{nonlinear, spm}} = \gamma P L \tag{2.6}$$

With L the length of the medium, P the peak power of the pulse and ϕ the phase of the light. As the intensity of a pulse at a given location varies with time, so too does the nonlinear phase shift caused by SPM vary over time. This time-varying phase shift is in effect the same as the generation of new frequency or wavelength components.

SPM is expected to continuously broaden the bandwidth of pulse, as long as the intensity of the pulse remains large enough for the Kerr effect to be significant. When propagating in an anomalous dispersion medium the effects of SPM can actually be compensated by the effects of dispersion itself. This is of high interest in anomalous supercontinuum generation as this is what enables the formation of solitons [24], which are discussed more in Section 2.2.3 below.

Cross-Phase Modulation (XPM)

Cross-Phase Modulation (XPM) is a nonlinear processes very similar to SPM. It too describes how the phase of a pulse is modulated by light, but instead of the intensity of a wave influencing itself, a wave is influence by the interaction with another wave. This is possible as the Kerr effect has an influence on the light through the (shared) material [31]. XPM leads to a phase shift very similar to that of Equation 2.6:

$$\phi^{(1)}_{\text{nonlinear, xpm}} = 2 \cdot \gamma P^{(2)} L \tag{2.7}$$

Where the superscripts identify unique waves. For the influence of waves between each other to be constructive, phasing matching of the propagation constants is required. For supercontinuum generation, like SPM, XPM is expected to have an influence in generally broadening the spectrum.

Four-Wave Mixing (FWM)

Four-Wave Mixing (FWM) is a nonlinear process that involves the interaction of three light waves that generate a new wavelength component [32], [33]. The new wavelength component lies at a phase matched frequency that is the sum- or difference-combination of the three incoming waves. Some of the incoming waves excite the material to a higher state, which then relaxes in a combination of waves consisting of both existing frequencies and newly generated frequencies. Figure 2.5a shows a diagram of what is called difference-frequency generation where the new frequency components f_4 has a frequency:

$$f_4 = f_1 + f_2 - f_3 \tag{2.8}$$

Figure 2.5: Schematic overview of the energy levels associated with Four-Wave Mixing. a) Non-degerate FWM; b) Degenerate FWM

Note that many more combinations are possible. This is an example of non-degenerate FWM where all wavelengths are unique. When two photons with the same wavelength interact in FWM, it is called degenerated FWM. In principle any linear combination of f_1, f_2 and f_3 is possible, as long as the phase matching conditions allows it. Degenerate FWM is often used for selective generation of sidebands. The degenerate wave is then typically called the pump, which in combination with a signal can generate a converter on the opposing side of the pump, described as:

$$f_c = 2f_p + f_s \tag{2.9}$$

Aside from the modelling through excitement and relaxation of electrons, FWM can also be described by side-band generation through a time-varying refractive index due to the Kerr effect. When two waves with differing frequencies propagate through a material, the intensity of the combines waves will vary over time with the

beat frequency between the two waves, see Figure 2.6. Through the Kerr effect, this varies the refractive index of the material with the beat frequency as well. This causes and frequency shift of the waves present inside the material, modulated at the beat frequency, which in turn generates frequencies at the input frequencies $\pm$ the beat frequency.

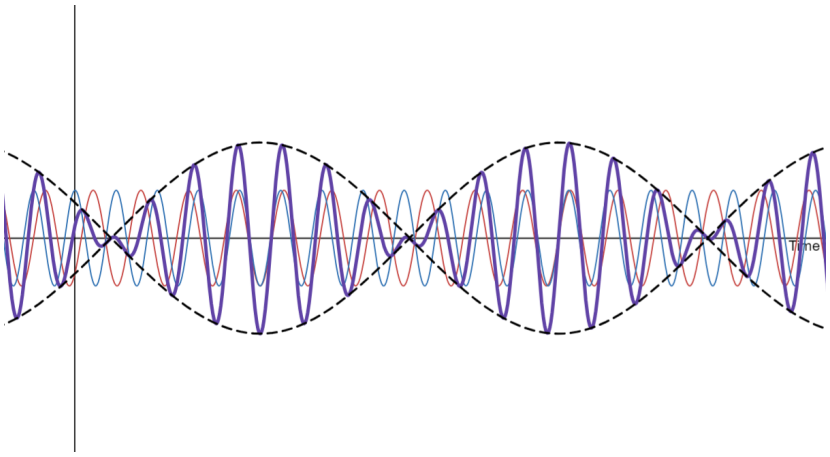

Figure 2.6: Two waves with offset frequencies (background, red and blue) interfering to crease a wave with varying envelope (foreground, purple and black).

For new wavelength components to continue there is a phase matching condition that needs to be satisfied (otherwise the newly generate waves would destructively interfere). This phase matching conditions is described as [34]:

$$\Delta\omega^2\beta_2 + \gamma P \approx 0 \tag{2.10}$$

Where $\Delta\omega$ is the spacing between waves, also called the beat frequency, and γP is the nonlinear phase shift. From this condition it is clear that for the highest efficiency of FWM β_2 needs to be negative, as the nonlinear phase shift will always be positive. In other words, for FWM to be most efficient, the light needs to propagate in the anomalous dispersion regime. For this reason, FWM can have a large influence on the spectrum in anomalous supercontinuum generation, in practise especially when β_2 is close to the zero dispersion wavelength. Through FWM a large number of new distinct frequencies can be generated as long as enough 'seeds' or starting waves are present. Because of the phase matching condition, FWM would have a limited influence in normal dispersion supercontinuum generation.

2.2.3 Soliton dynamics and Dispersive Waves

Soliton dynamics play an important role in anomalous supercontinuum generation. They are stable wave packets that can keep their shape over long distances, or undergo fission and dramatically broaden the spectrum of a pulse. First discovered in waves in canals [35] they now play an important role in many applications. Solitons are for example widely used in telecommunications as their stability allows for long distance transmission, and are of great importance to nonlinear optics as well [36].

Soltions are formed on a precisely balanced cancellation between SPM and GVD. In a medium the group velocity dispersion will lead different frequencies of light travel to travel at different speeds, which results a pulse of light spreading out temporally. In a sufficiently nonlinear material however, and with a pulse of the right shape, the effects of SPM can cancel out the spreading of the pulse, keeping it components travelling at the same speed [24], see Figure 2.7. As SPM will induce a shift where high energy waves will travel slower and low every waves will travel faster, solitons can only be created in a medium with anomalous dispersion, where dispersion causes high energy waves to travel faster and low energy waves to travel slower.

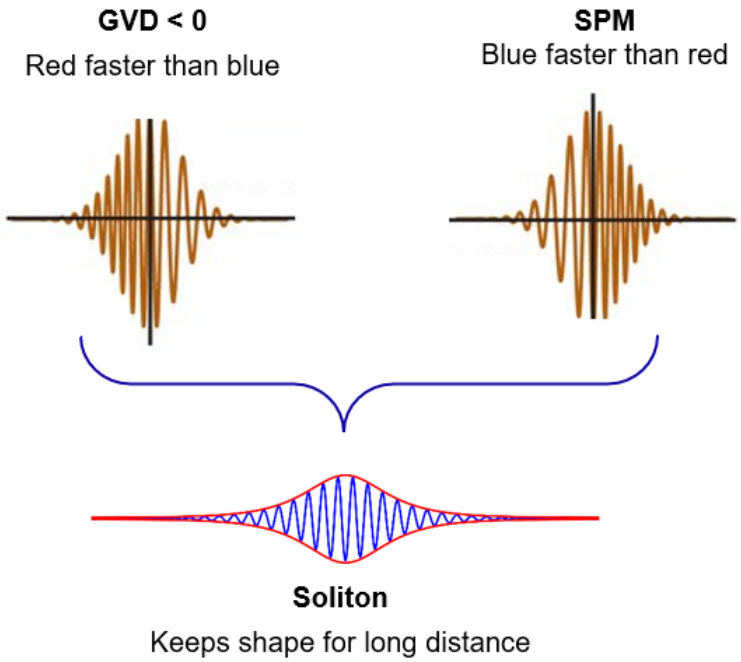

Figure 2.7: A schematic overview of how anomalous GVD and SPM can cancel out to allow the propagation of solitons. Image adjusted from: [37].

Solitons can be described by their soliton number expressed as:

$$N = \sqrt{\frac{L_D}{L_{NL}}} = \sqrt{\frac{2\pi \cdot n_2 \cdot P_0 \cdot T_0^2}{|\beta_2| \cdot \lambda \cdot A_{\text{eff}}}} \tag{2.11}$$

Where:

- L_D is the dispersion length.
- L_{NL} is the nonlinear length.
- T_0 is the pulse duration, also called pulse width. Typically measured in fs.
- P_0 is the peak power of the pulse.

For N=1 a fundamental soliton is formed. For N > 1 higher order solitons are formed, which can interfere with each other to form oscillatory shapes, see Figure 2.8. Higher order solitons are especially interesting with regards to SCG as they can undergo soliton fission. This is a processes where the higher order soliton is broken up into multiple fundamental solitons, each with their own temporal and and spectral shapes [38]. This generates new wavelengths and can drastically broaden the spectrum of a pulse, especially as the new wavelengths can interact with each other to broaden the spectrum even more through processes as described in Section 2.2.2.

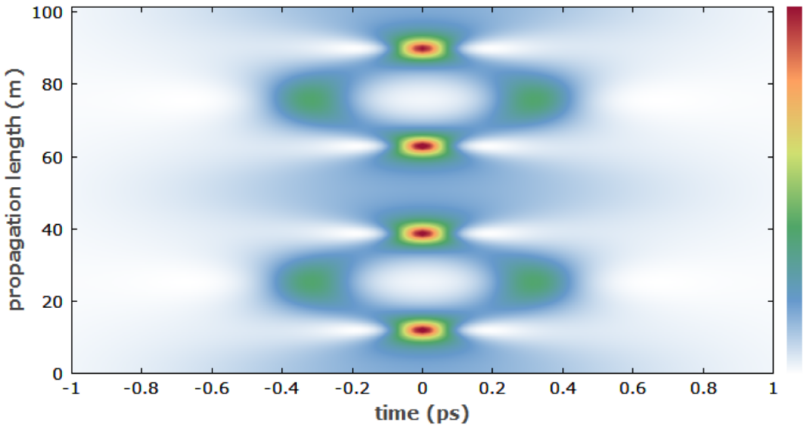

Figure 2.8: Temporal evolution of a third-order soliton. Image source: [39]

Dispersive Waves

Aside from the spectral broadening, another property of solitons is that they can shed some of their energy while being in the process of conforming to their optimal shape. The resulting light is called a dispersive wave because it is no longer strongly influenced by SPM, as its peak power will be much lower compared to that of the soliton [40]. The wavelength of this propagating dispersive wave can be predicted using the matching equation [41]:

$$(\beta_{dw} - \beta_s) = (\omega_{dw} - \omega_s) \cdot \frac{d\beta_s}{\omega_{dw}}, \tag{2.12}$$

Where the subscript s denotes the soliton (or pump) and dw the dispersive wave.

At this dispersive wave wavelength there will be relatively high power in the generally broadened spectrum, as the direct energy transfer between the soliton and the dispersive wave is typically much more efficient than the energy transfer through multiple nonlinear processes. See Figure 2.9 for an example of a dispersive wave inside a spectral evolution of SCG. As the propagation constant β and its derivative can be influenced by changing the geometry of a waveguide, the expected location for a dispersive wave can also be influenced by changing the geometry of a waveguide. In other words, through dispersion engineering the location of the dispersive wave can be chosen. This is a powerful tool as it allows to selectively generate high power bands in a supercontinuum for efficient energy conversion between the pump and an arbitrary wavelength. This is why the expected location of dispersive waves is taken into account when designing the chips.

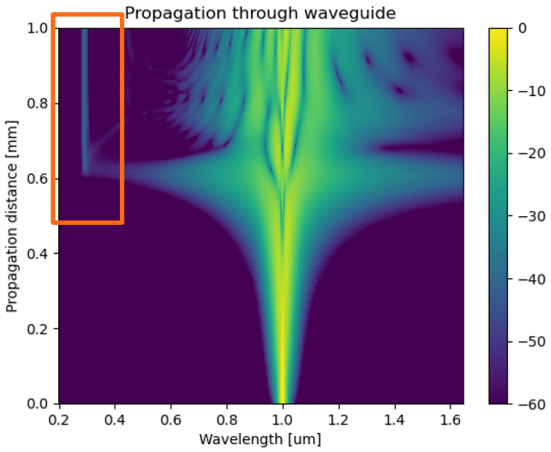

Figure 2.9: An example of the generation of a dispersive wave (outlined box). Notice how the intensity suddenly spikes much higher compared to surrounding wavelengths.

2.3 Chip Design

The section will document the design process for the SCG photonic chips, as well as cover different layout components presented in the design layout. The goal of the designs is to create PICs that allow for a multitude of (future) experiments with regards to SCG in Al_2O_3, including SCG that can reach into the UV and the placing of dispersive waves through dispersion engineering.

In all simulations and calculations, the Sellmeier values from the ALUVIA design manual were used to determine the refractive index n of the Al_2O_3. With those, n is described as:

$$n(\lambda) = \sqrt{\epsilon_\infty + \frac{A\lambda^2}{\lambda^2 - E^2} - P\lambda^2}, \tag{2.13}$$

with the wavelength λ in µm and:

- $\epsilon_\infty = 1$
- $A = 1.912$
- $E = 0.09566$
- $P = 0.00306$

The SCG chips have been designed to operate at a pump wavelength of 1064 nm, the choice of which is explained in more depth in Section 2.3.1 below. At 1064 nm, the refractive index of Al_2O_3 is $n = 1.71$. The thickness of the Al_2O_3 structure is 451 nm $\pm 5\%$, set by the wafer available at ALUVIA. The design choices were mostly governed by this and available laser sources.

Although the chip are designed to operate at a pump wavelength close to 1 µm, in the final stage before fabrication, extra edge couplers were added to also support lasers operation at 1.55 µm as a backup against unforeseen circumstances (which turned out to work in our favour). The SCG chips are also designed to be partially uncladded as a SiO_2 cladding prevents the waveguide from being in the anomalous dispersion regime. The input edges of the chips will always remain cladded, facilitating a symmetric mode allowing for lower coupling losses, see also Section 2.3.3. Through Lumerical MODE simulations, it was found that uncladded waveguides on the available wafer, at a wavelength of 1064 nm, are single mode between widths of approximately 0.72 µm and 1.55 µm, assuming a sidewall angle of 70°, as specified in the ALUVIA design rule manual. See Figure 2.10 for a schematic representation of the waveguides.

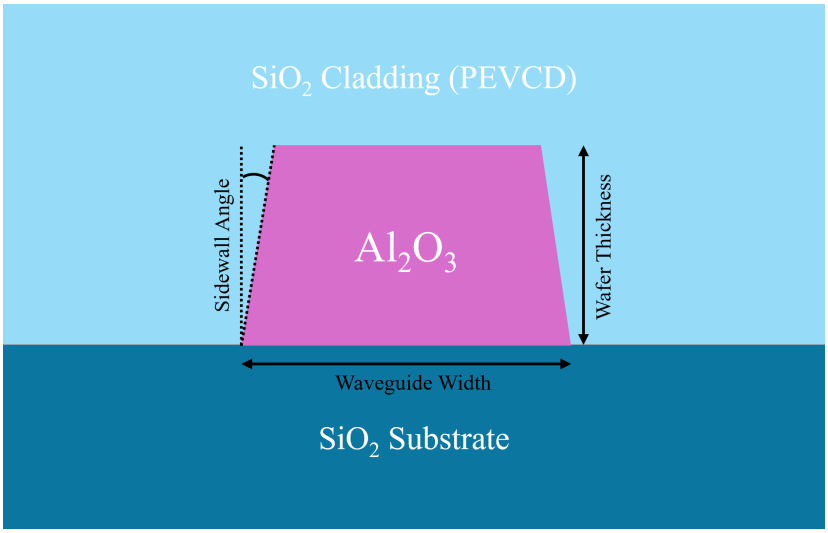

Figure 2.10: A schematic representation of an Al_2O_3 waveguide. The viewing direction is parallel to the propagation direction.

2.3.1 Anomalous dispersion region

As discussed in Section 2.2, the group velocity dispersion β_2 needs to be negative at a specific wavelength for it to be in the anomalous dispersion region. Anomalous dispersion is essential to allow solitons and their associated dramatic spectrum broadening and dispersive waves.

The effective refractive index n_{eff} for a specific waveguide is found through MODE simulations in Ansys Lumerical. With this, the propagation constant β can be calculated using:

$$\beta = n_{\text{eff}} \frac{2\pi}{\lambda}$$

From β, the GVD β_2 is calculated (see Equation 2.5). For the determination of the design wavelength, these steps were repeated for a range of waveguide widths from 0.2 µm to 5 µm, with an assumed thickness of 451 nm for the Al_2O_3 wafer, and a wide range of wavelengths. Figure 2.11 shows the resulting β_2 values. This graph displays the GVD of many waveguide geometries (fixed thickness and varying width, see Figure 2.10), for a wavelength of light on the y-axis. The color/intensity scale indicates the GVD value, and the dotted lines separate the anomalous- and normal-dispersion regions.

Notice how, for uncladded 451 nm thick Al_2O_3, there is a considerable range of wavelengths for which the dispersion regime is anomalous. This figure shows that a pump wavelength of around 780 nm would likely be ideal as it is close to the zero-dispersion wavelength (where nonlinear processes tend to be more efficient, see

Section 2.2). Wavelengths above 1500 nm, such as those in the telecom C-band, will always be in the normal dispersion regime given the wafer thickness. Using information from Figure 2.11 and considering the general availability of high-power pulsed lasers, the choice was made to design for 1064 nm. This wavelength lies squarely in the anomalous dispersion regime (providing some tolerance to fabrication variances), while allowing for low-dispersion waveguides on the smaller end of the single-mode regime. Notably, this wavelength was also available through a laser source at LPNO research group from the University of Twente.

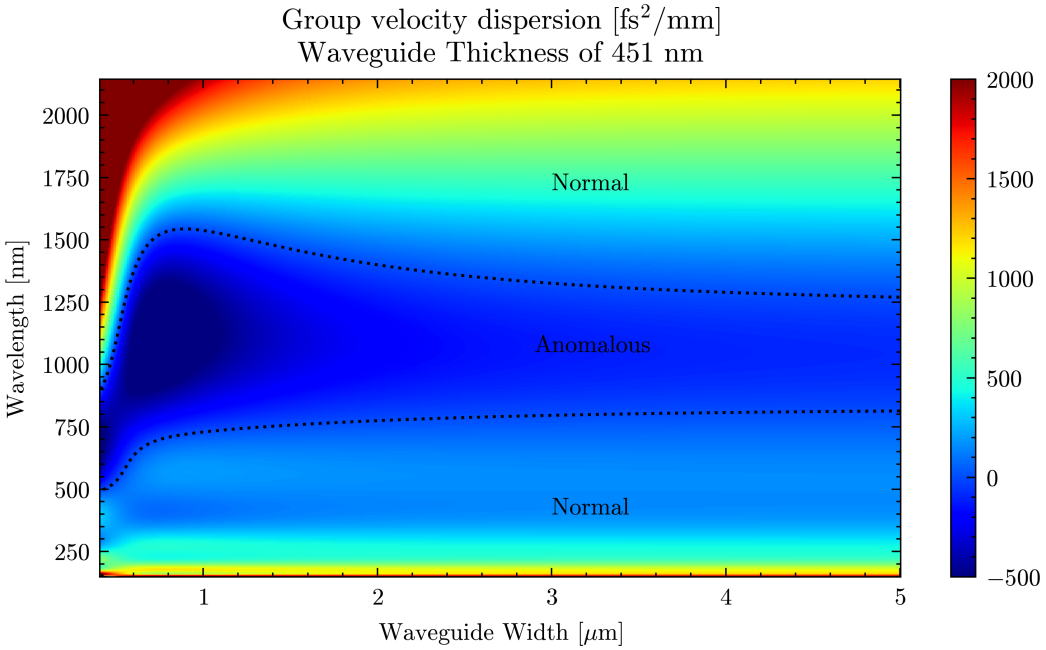

Figure 2.11: Simulated group velocity dispersion values for uncladded Al_2O_3 at thickness of 451 nm. Dotted lines indicate the boundary between normal and anomalous dispersion (zero-dispersion wavelengths)

2.3.2 Dispersive Wave Phase Matching

The dispersive wave phase matching condition (see Equation 2.12) is solved similarly to the above method. The propagation constants for the modes of the Al_2O_3 waveguides are calculated for a range of wavelengths from 0.17 µm to just above the design pump at 1.2 µm. With this data, the dispersive wave phase matching condition can be solved for a range of waveguide widths. Figure 2.12 shows at which wavelength a dispersive wave is expected (x-axis), given a simulated waveguide width (y-axis) and a 1064 nm pump. The dotted lines indicate the boundaries of single- and multi-mode propagation. Note that having an expected location does

not mean there will always be a dispersive wave at this spectral location; it only highlights where the phase matching condition would allow dispersive waves, assuming solitons arise and can shed enough energy to reach the correct wavelength (see Section 2.2).

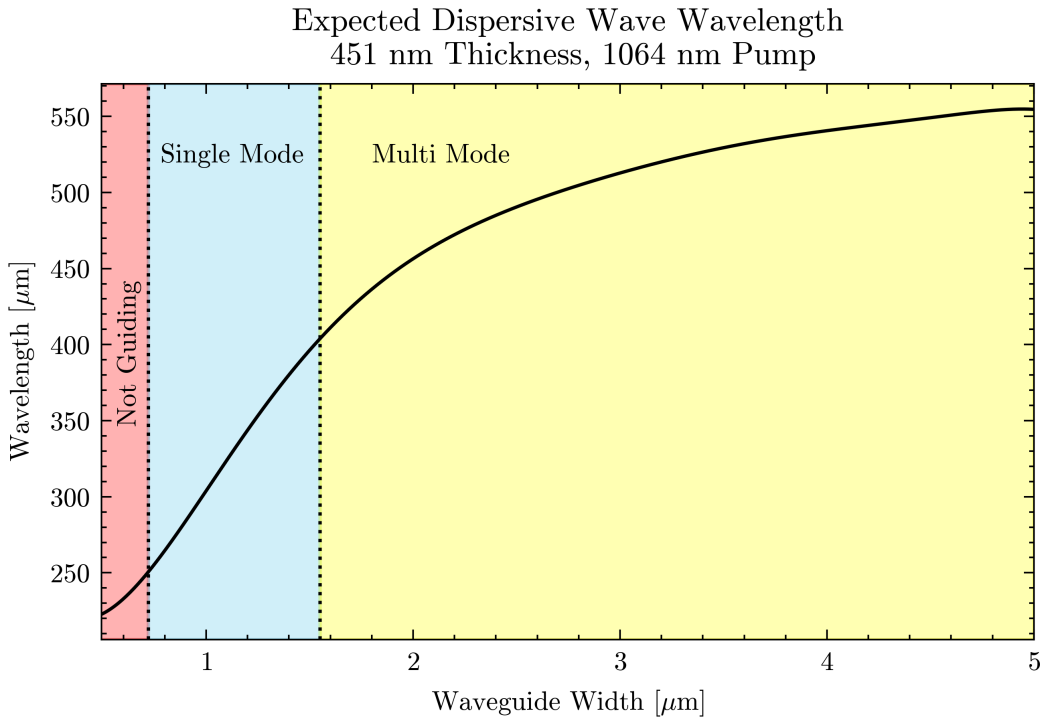

Figure 2.12: Dispersive wave phase matching locations for uncladded Al_2O_3 waveguides. The x-axis show the expected location for a dispersive wave. The dotted lines indicate the boundary between single- and multi-mode propagation.

Looking at Figure 2.12, the dispersive wave location ranges from very close to the 170 nm bandgap of Al_2O_3 to around 400 nm in a nearly linear fashion. After this, the dispersive wavelength asymptotically approaches approximately 550 nm. The smallest guiding waveguide exhibits phase matching at around 250 nm, making this the lower limit of dispersive wave generation for this wafer. The upper limit for single-mode pump propagation lies close to 400 nm.

The choice was made to fabricate a large number of waveguides, spread out in widths, to allow extensive testing in future research for a holistic picture of SCG and dispersive waves. This also provides flexibility to switch between closely related waveguide by simply switching to another geometry. Finally it also provides a form of tolerance in case of fabrication variances or failure..

In total, 10 waveguides were selected in the single-mode region, spanning from 0.6 µm to 1.5 µm with a spacing of 0.1 µm. Another 20 waveguides were selected in the multi-mode region, spanning from 1.6 µm to 5.78 µm with a spacing of 0.22 µm. Finally, 6 waveguides were placed from 6 µm to 11 µm, with a spacing of 1 µm. More details on the selected waveguides, including edge couplers, can be seen in Appendix A.

2.3.3 Layout

Each PIC was given a die area of 1 cm by 3 cm. Every chip can support up to 72 waveguides with this size, taking into account the need for a bend to reduce stray light at the output, and the spacing of the waveguides. There were a total of four chips available for this project. Figure 2.13 shows an overview of the layout of the chip. The oblong chip size was chosen to provide a long enough interaction length for the chips to be able to exhibit SCG. From left to right there will be an edge coupler to couple in light from free-space or fibers onto the chip (this includes a long adiabatic taper), followed by a double 90° adiabatic (Euler) bend, and then a straight section.

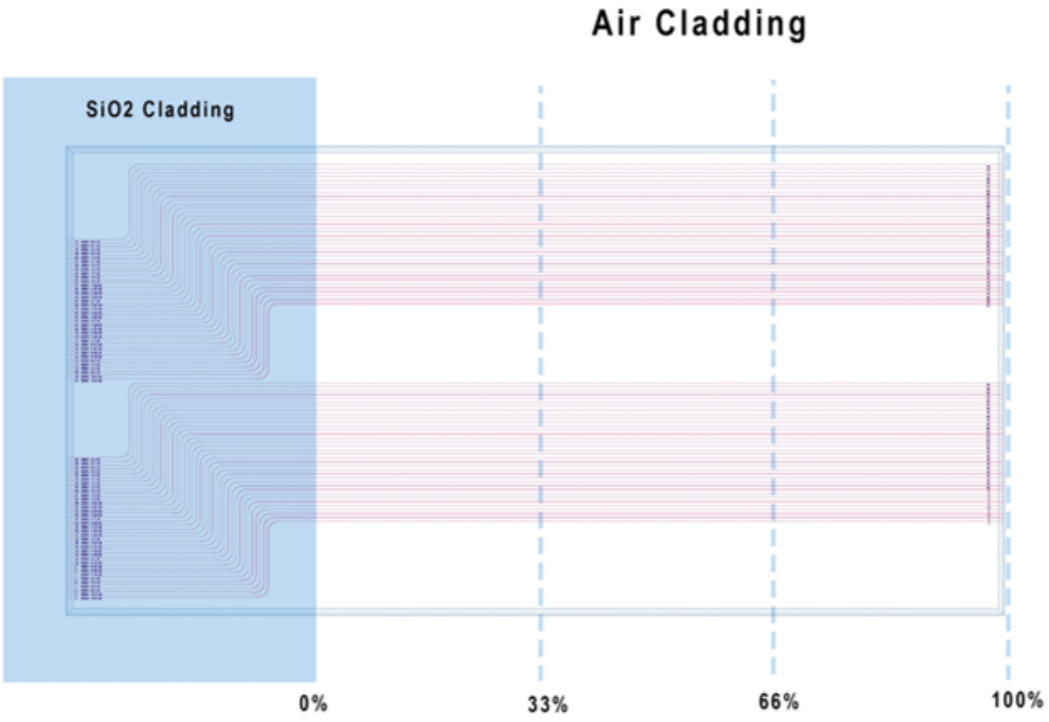

Figure 2.13: Schematic layout of the PIC.

The edge couplers and bends will always be covered with a SiO_2 cladding to reduce losses for the input tapers and to initially suppress anomalous SCG (which can only occur in uncladded regions). The final straight section is meant to host the anomalous SCG. In the four chips available, each will have a different amount of cladding on this last straight section. This is to have the ability to compare anomalous propagation lengths within the same chip design. The cladding of the four chips ranges from 0% to 100% cladding in the final section, denoted by the dotted lines in Figure 2.13. The two bundles of waveguides on the chip, see Figure 2.13, will be identical except for the edge coupler: the topmost bundle has an edge coupler for 1 µm light, the bottom one for 1.55 µm light. Note that there are no edge couplers at the outputs. This is to maximize the supported spectrum of light coming from the chip, which can be captured using a large mode field diameter fiber at the output.

The chosen waveguide diameters can be seen, together with further information about which waveguides are single- or multimode in their cladded and uncladded regions, in Appendix A. The choice of waveguides was made based on the simulated data from Sections 2.3.1 and 2.3.2.

Edge Couplers

Edge couplers are an essential structure when coupling in light, especially as there is a wide range of waveguide widths which each would have their own effective mode area. They are designed to minimize the coupling losses of a device by matching the mode fields of the incoming light and that of the waveguide. The mode field diameter of the edge couplers is designed to match the mode field diameter of the incoming light (be it either from free-space or fiber). This width, at the input edge of the chip, is then tapered to the designed width of the waveguide over a long range, e.g. 1.5 mm, to adiabatically transfer the light from the input to the waveguide. Figure 2.14a shows a schematic overview of an edge coupler. Notice that in this design the starting width of the edge coupler is smaller than that of the normal waveguides, as the mode diameter of the input light is typically large compared to waveguide structures.

The edge couplers were designed using the MODE solver of Ansys Lumerical. Figure 2.14b shows the simulated performance of an edge coupler with a 1.5 mm length against different incoming mode areas. The peak power coupling is at approximately 82% and lies close to the fiber mode field diameter. Notice how the power coupling is relatively flat around this peak, meaning that the edge coupler still has some margin in which it is effective, around the design wavelength.

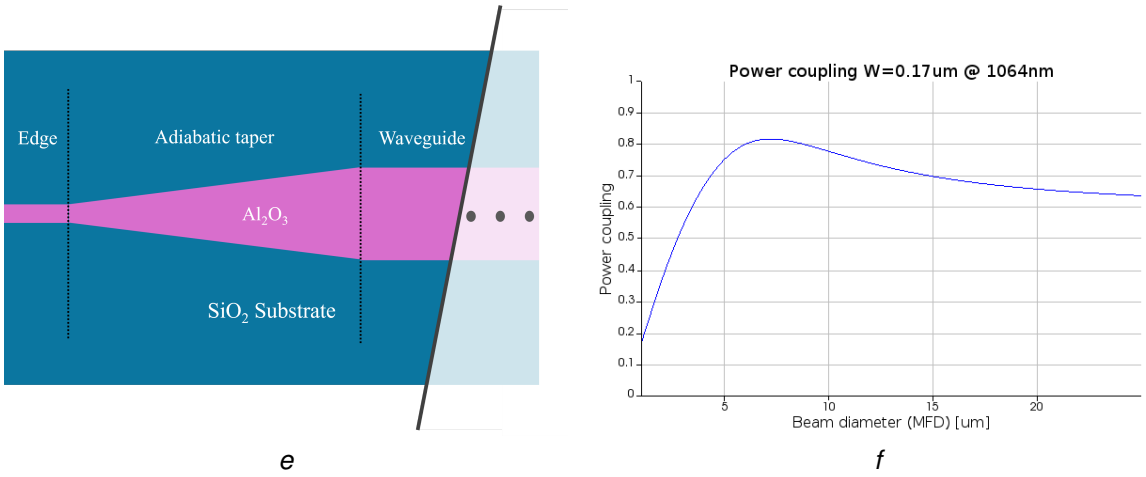

Figure 2.14: a) Schematic of an edge coupler, including an adiabatic taper to the waveguide; b) The power coupling performance of the edge coupler, simulated using Lumerical MODE.

Euler Bends

The bends in the layout are necessary to offset the input and output of the chip to minimize stray light entering the output fiber. The two 90° bends are both adiabatic Euler bends, which means that they have a gradually increasing curvature, in comparison with a normal circular bend where the radius directly switches from ∞ to a fixed value. Adiabatic bends are used because they minimize the loss in the bends caused to the mode mismatch between the straight and curved section of the waveguides. The minimum bend radius was chosen based on the ALUVIA design manual and the design of the Euler bends was based on the methods described in [42].

Cladding

The cladding that is placed on part of the chips is a Plasma-Enhanced Chemical Vapor Deposition (PECVD) SiO_2 cladding deposited on parts of the chips using a shadow mask. The refractive index can be determined using the following Sellmeier coefficients and Equation 2.13.

- $\epsilon_\infty = 1$
- $A = 1.117$
- $E = 0.09161$
- $P = 0.00882$

At the design wavelength of 1064 nm, this gives a refractive index of $n_{\text{clad}} = 1.45$.

2.3.4 Fabrication

The Al_2O_3 structures were defined on a 451 nm thick film using electron-beam lithography (EBL). A negative resist of 1000 µC/cm^2 was patterned and reactive ion-etching (RIE) was used to define the waveguides and rings. The film deposition was performed using reactive magnetron sputtering on a 10 cm diameter silicon wafer with an 8 µm thermal oxide layer. After this, an 8 µm thick SiO_2 cladding was deposited using Plasma-Enhanced Chemical Vapor Deposition (PECVD) on specific regions using a shadow mask. Deposition and lithography were performed in the MESA+ Nanolab following procedures outlined in [43], [44]. This process is identical, with the exception of the used wafer, for the micro-ring resonator fabrication presented in Chapter 3.

The fabrication was mostly successful. The waveguide are nicely defined and text layer is clearly visible. Figure 2.15 shows a few example images taking with a microscope. The quality of these waveguide is representative of the majority of the four chips.

There were a small number of exceptions where a section of the waveguide was not defined. Because the missing sections do not show any rough edges or scattering, it was believed that they were not waveguide breaks, but more likely fabrication defects. An example can be seen in Figure 2.16. These very occasional defects did not pose a problems to the experiments.

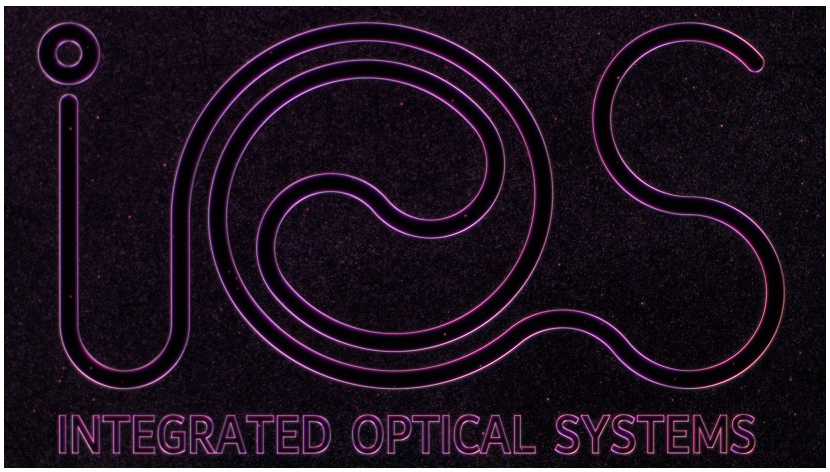

(a)

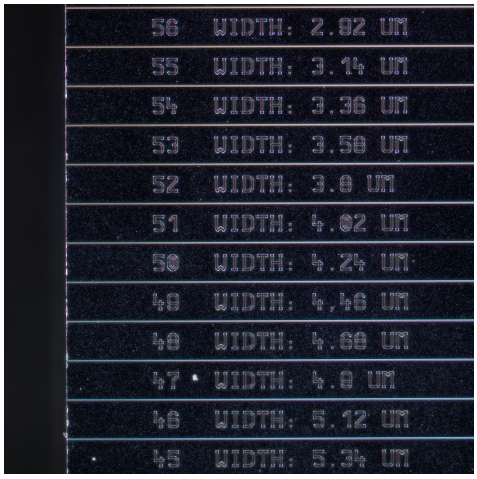

(b)

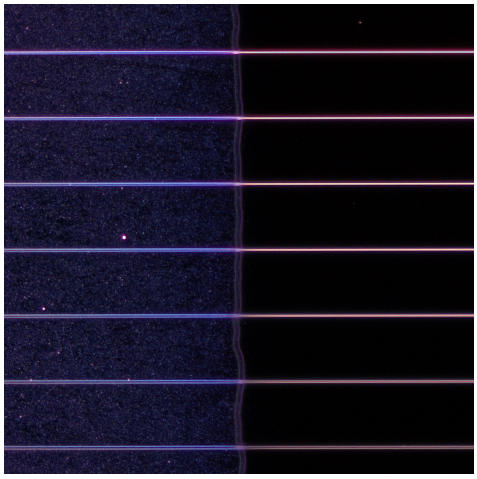

(c)

Figure 2.15: Some example photographs of the PICs, taking with a microscope. a) the IOS research group logo; b) The edge of the chip, showing a clearly legiable text layer; c) The transistion between cladded and uncladded sections on chip.

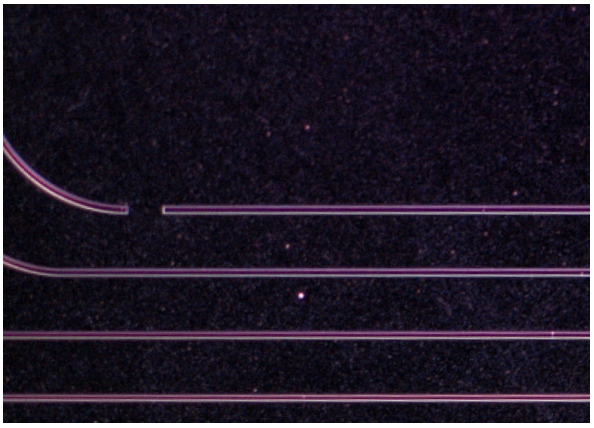

Figure 2.16: Photograph through a micrscope of the occasional fabrication defects.

2.4 Simulation performance

During the design phase, multiple nonlinear simulations were run to demonstrate the theoretical capabilities of the Al_2O_3 waveguides. These simulations are based on the opensource Pychi [45] library in Python. This library contains a custom 5^{th} order solver, designed to simulate short pulses through nonlinear materials. It is capable of simulating a wide range of nonlinear effects, including all mentioned in Section 2.2. The pulses used for simulation have a width of 130 fs at 1064 nm and have an average on-chip power of 95 mW, with a repetition rate of 40 MHz. Together giving a pulse energy of 2.37 nJ. These values are based on the Ekspla LightWire FF200 laser and a 5 dB coupling loss. The simulations cover a wavelength range of 170 nm to 2200 nm over a propagation distance of 3 mm with a step size of 6 µm. Figures 2.17 and 2.18 show the time-domain and wavelength-domain evolutions for two waveguides, as well as their final spectra. The waveguides chosen for simulations have a with of 0.8 µm and 1.4 µm. This places them at the lower and upper edge of the single mode regime for 1064 nm light (these are waveguides 3 and 23 on chip, please see Appendix A).

For the 0.8 µm width, the waveguide exhibits a GVD of -678 fs^2/mm and a soliton number of 14. The phase matching condition in Equation 2.12 predicts a dispersive wave at 268 nm, see Figure 2.12. A dramatic broadening of spectrum can be seen after approximately 0.7 mm of propagation in Figure 2.17b, which is the point of soliton fission. Here the -40 dB intensity just crosses into the UV reaching from 400 nm to 2100 nm. Please note that the intensity is relative to the peak of the *input* pulse, and not relative to the local maximum. A dispersive wave is also visible in the waveguide evolution. It comes into existence after the soliton fission, which is expected as the shedding of energy from the solitons creates the dispersive wave. This dispersive wave remains stable even after propagation. The final peak intensity of the dispersive wave is -25 dB, relative to the peak intensity of the input pulse. Its location is at 250 nm, which is slightly lower than the predicted 268 nm.

For the 1.4 µm width, the waveguide exhibits a GVD of -283 fs^2/mm and a soliton number of 16. The phase matching condition in Equation 2.12 predicts a dispersive wave at 415 nm, see Figure 2.12. For this waveguide the dramatic broadening can be seen after approximately 1.2 mm of propagation in Figure 2.18b. The difference between the soliton fission locations between the waveguides can be explained by their difference in effective area. The smaller waveguide will have a higher power density and thus a higher effective nonlinear coefficient. For the 1.8 µm waveguide the bandwidth at -40 dB at soliton fission is even broader, reaching from approxi-

mately 300 nm to outside the simulation window above 2200 nm. Again a dispersive wave is clearly visible. Notable is how this dispersive wave has a larger bandwidth compared to the dispersive wave in Figure 2.17. Also notable is how its location is considerably blue-shifted at 350 nm compared to the predicted 415 nm. This might be due to red-shifting of the solitons, which would change the phase matching condition [46].

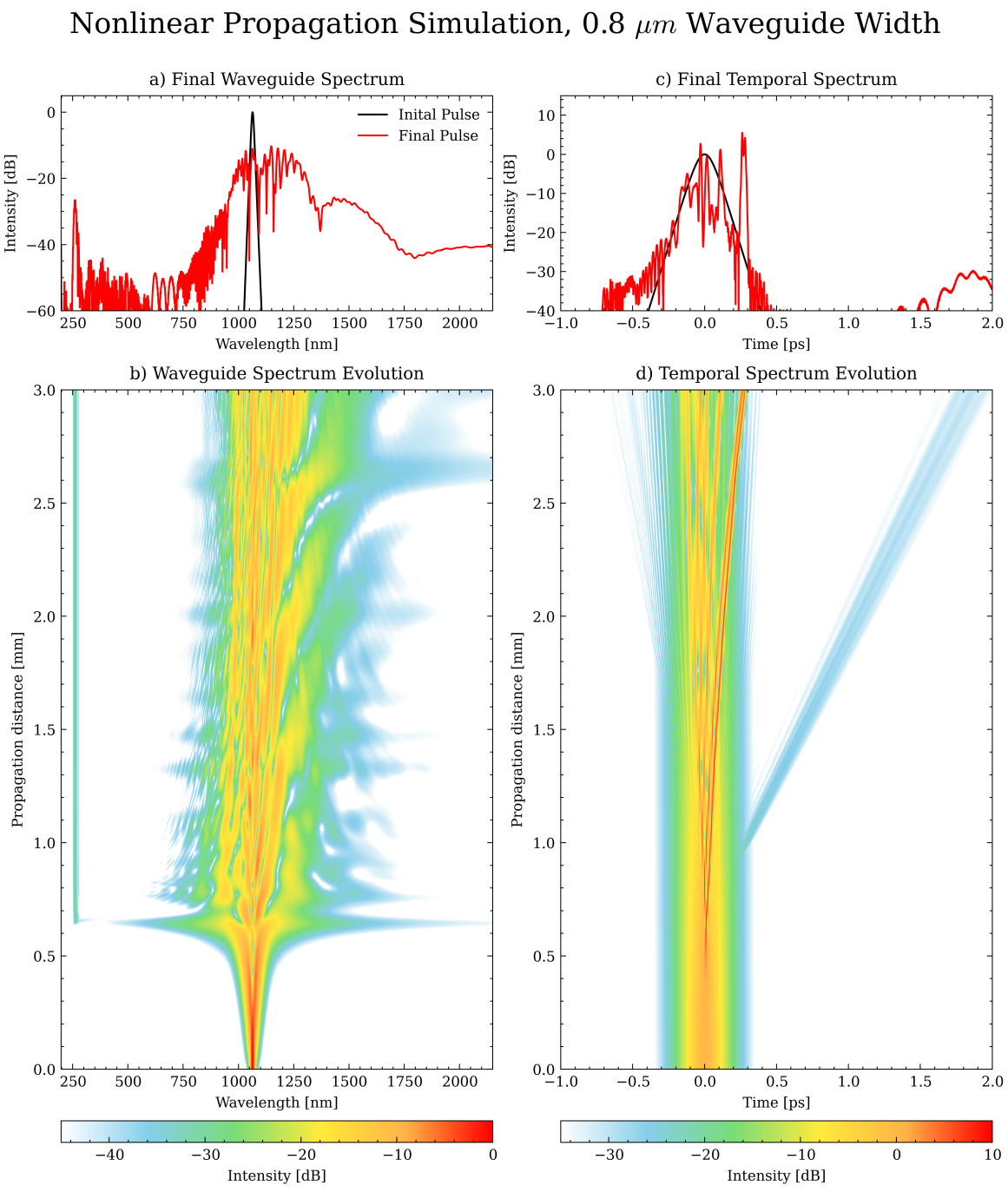

Figure 2.17: The above images shows the evolution of both the wavelength and temporal spectra of a sech^2 pulse, simulated in 0.8 µm Al_2O_3 waveguide. a) Wavelength spectrum at the end of propagation; b) Evolution of wavelength spectrum through waveguide; c) Temporal spectrum at the end of propagation; d) Evolution of temporal spectrum through waveguide.

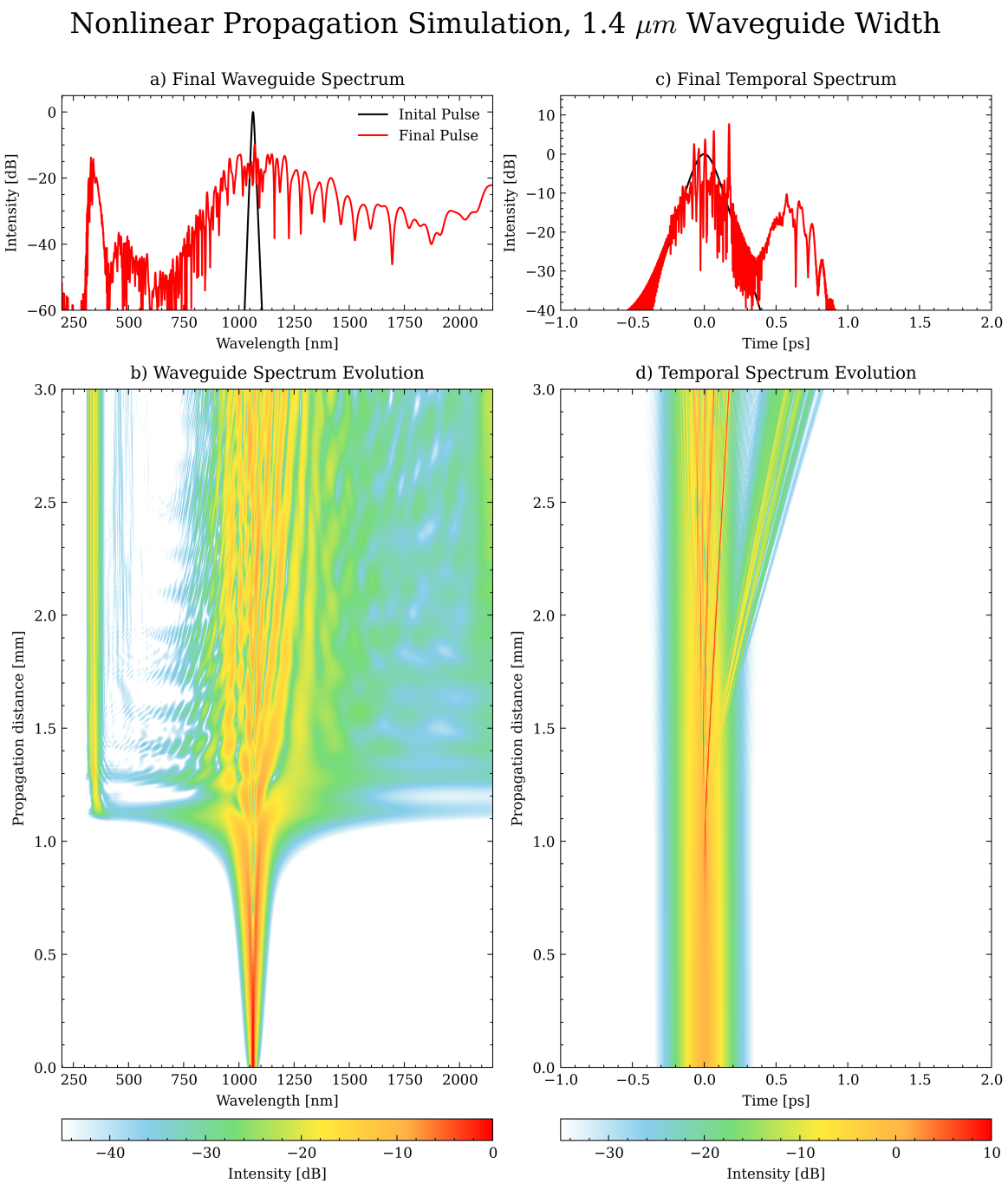

Figure 2.18: The above images shows the evolution of both the wavelength and temporal spectra of a sech^2 pulse, simulated in 1.4 µm Al_2O_3 waveguide. a) Wavelength spectrum at the end of propagation; b) Evolution of wavelength spectrum through waveguide; c) Temporal spectrum at the end of propagation; d) Evolution of temporal spectrum through waveguide.

2.5 Experimental results

The following section will detail the experimental methods used, as well as the experimental results. Unfortunately the intended 1 µm laser source has broken before the start of measurements, and could not be repaired within the time-scope of the project. Because of this, the backups edge couplers were used to couple in light from a 1544 nm FF ULTRA 1560 high-power pulsed laser (capable of pulse energies of up to 28 nJ). As discussed in Section 2.3.1, the wavelength of this laser is too high to propagate in the anomalous dispersion regime, this limits us to only a potential broadening predominantly due to SPM. Nevertheless, this should still yield interesting quantities like the pulsed damage threshold of the material and visible confirmation of nonlinear processes in Al_2O_3 (and of course, valuable lab experience).

2.5.1 Ekspla 1 µm laser

The Ekspla LightWire FF200 1064 nm posed as the original guide for the design of the chips. For this laser a characterisation was planned, due to an extended period of inactivity. This characterisation was important as the properties of the laser-pulse can have a strong influence of the measured processes, and can change over time. Aside from this, and as proved in this project, a characterisation can discover problems with the laser in an earlier stage of the experiments. The characterisation originally included an average power measurement using a photodiode and measuring the pulse duration using an autocorrelator, which is a device capable of resolving ultra-fast pulses of light (which for a photodiode is too slow).

For the pulse duration measurement an APE PulseCheck autocorrelator was used, see 2.19a. The processed involved aligning the IR beam of the laser to the input of the PulseCheck, this was sped up considerably with the help of a phone camera that happened to not fully filter out the 1 µm light, see Figure 2.19b. The settings for delay, beam distance and focus were adjusted according to the manual. Unfortunately no pulses coming form the laser were detected, with the output of the PulseCheck only indicating noise, see Figure 2.19c.

The average power of the laser was measured at 188 mW, approximately 2/3 of the 300 mW expected average power. To look further into possible problems, the pulse train output of the laser (with an expected repetition rate of 40 MHz) was connected to an oscilloscope, but showed no pulsing behavior. With this, it was con-

firmed that the laser would not be able to supply the required high-power pulses and was deemed broken.

The secondary laser, the 1544 nm FF ULTRA 1560, was already in use in the lab and had extensively been tested, so no autocorrelator measurements were performed. A detailed Quality Control can be found in Appendix B.

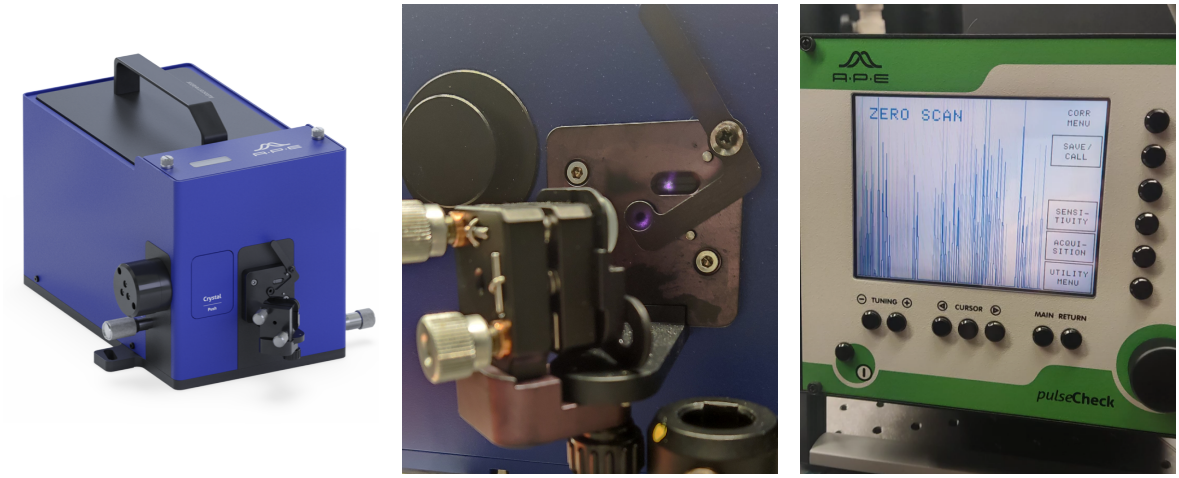

(a): **(b):** **(c):**

Figure 2.19: From left to right: **a)** APE PulseCheck (image from [ref]); **b)** IR beam made visible through a phone camera, used for alignment to the PulseCheck; **c)** Output of the PulseCheck showing only noise.

2.5.2 Methods

A high-power free space laser system (Toptica FF ULTRA 1560) was used for these experiments. This laser has a:

- central wavelength of 1544 nm;
- pulse duration (width) of 164.0 fs;
- repetition rate of 78.5 MHz;
- maximum average power 2.245
- free space beam diameter of 1.4 mm.

This together give a maximum peak power of 174.4 kW and a maximum energy per pulse of 28.60 nJ assuming a dominantly sech^2 pulse. For the full detailing of the performance of the laser, please see the Quality Control sheet in Appendix B.

Figure 2.20 shows a schematic overview of the setup used. An isolator is used to protect the laser from back-reflections into the source. An adjustable Half-Wave Plate (HWP) in conjunction with a Polarizing Beam Splitter (PBS) forms an adjustable attenuator for the signal. Any light that is changed from the pass-through polarization of the PBS by the HWP is reflected out of the system and caught in a beam stop. The continuing light is rotated back to TE polarization by a second HWP. An aspheric lens is used to focus the light into a beam diameter as close as possible to that of the designed edge couplers, see Section 2.3.3. The chip and the output fiber are placed on separate three degrees of freedom (DoF) stages. The laser beam can be controlled through various mirrors (not shown in the diagram). Figure 2.21 shows a photograph of the used three-DoF stages.

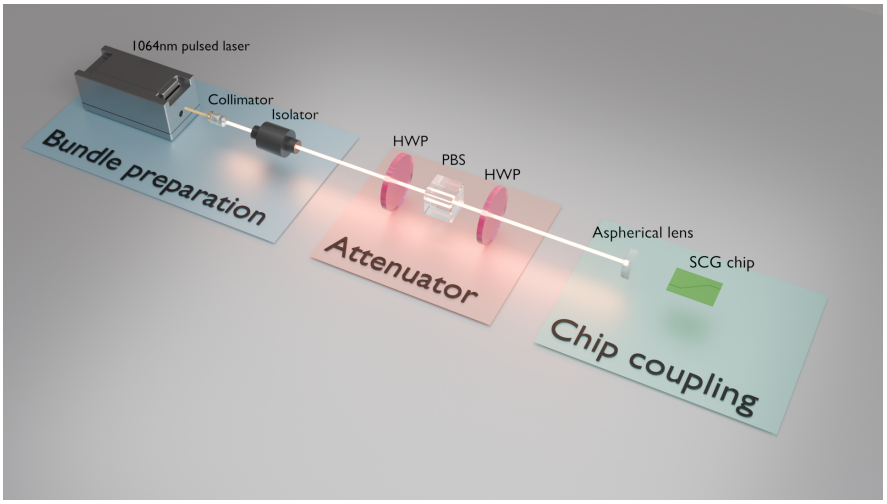

Figure 2.20: A schematical overview of the setup used for free-space SCG.

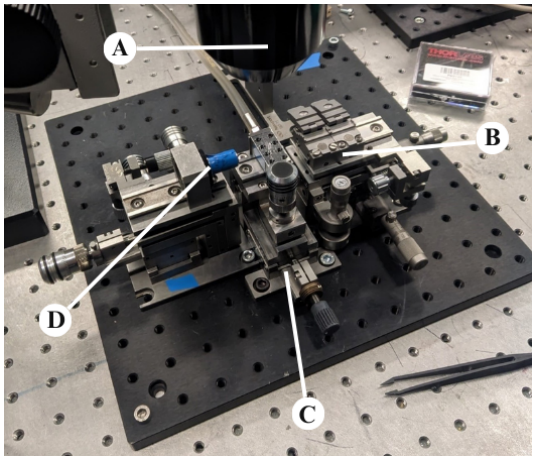

Figure 2.21: Photograph of the used stages with annotation.

For alignment to the chip, a visible green laser is injected into the system through

a dichroic mirror. The IR laser and the alignment laser are made to overlap with the help of a number of pinholes spaced between the second HWP and the aspherical lens in Figure 2.20. The reason this method was chosen over, for example, back propagation of an alignment laser through fiber coupling, is that there are no edge couplers at the end of the chip, making coupling in light for back propagation impractical.

Measurement Procedure

1. **Rough Alignment**
   The IR laser and the green alignment laser are first aligned using a number of pinholes and mirrors. The pinholes are adjusted to allow the IR laser to pass through. The alignment laser is then adjusted to also pass through all pinholes, with adjustments moving from the mirror closest to the alignment laser to the furthest. The chip is aligned to the alignment laser through a three-DoF stage and with the help of a microscope. Maximum coupling is determined by the amount of visible light scattering in the waveguides.

2. **Fine Alignment**
   Once the chip is guiding visible light, the alignment laser is shut off. Fine alignment is done with very low IR laser power (in the order of nW/μW) and optimized through a fiber power meter connected to the output fiber. The output fiber is first aligned to the chip using a microscope and then the system is adjusted in the following order: mirrors, chip stage, fiber stage. Where the last two are often repeated many times per mirror adjustment to determine the local optimised position.

3. **OSA Measurement**
   After fine alignment, the output fiber is connected to the OSA through a 99:1 splitter. The siphoned 1% is used to record the output power. The input power is measured in front of the aspherical lens using a free-space power meter. Following that, an OSA spectrum measurement is taken. Then the power is increased incrementally and the measurements repeat. For each step, the input and output powers are recorded, as well as the spectrum through the OSA.

Figure 2.22 shows a photograph with the green alignment laser in place. Notice how the light enters on the left side of the chip (top-left in the image), bends upwards, and then bends toward the output of the chip.

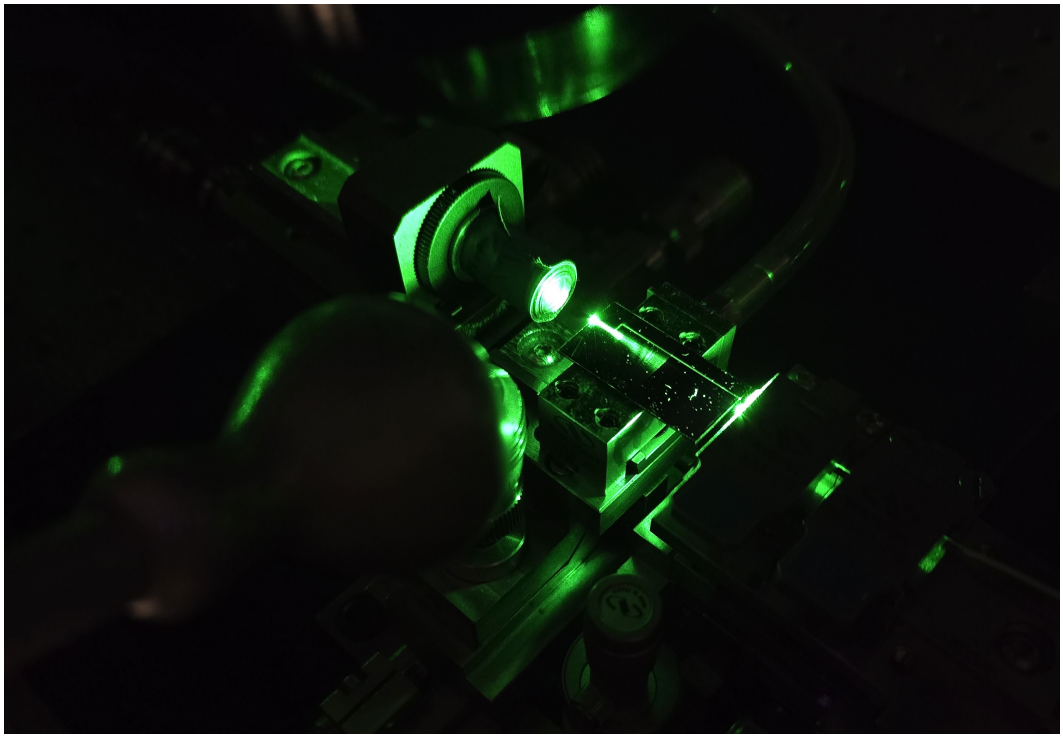

Figure 2.22: Photograph of alignment laser to chip

2.5.3 Results

The measurements shows in the section were done on waveguide 56 (see Appendix A for more information). This waveguide has a width of 3.58 µm and is uncladded, save for the in-coupling section, see Figure 2.13. Using the Toptica FF Ultra 1560 laser, a maximum averaged power before the chip of 1.7 W was set. After coupling losses, this resulted in an estimated maximum on-chip averaged power of 664 mW, together with a maximum peak power of 48.5 kW and a pulse energy of 8.47 nJ. Figure 2.23 shows multiple measurements taken on the same waveguide with increasing powers. The figure shows broadening of the pump spectrum, with a steadily increasing bandwidth. As all waveguides exhibit normal dispersion at wavelengths close to 1550 nm, this broadening is predominantly due to Self-Phase Modulation. At maximum power the chip shows an approximate 3x bandwidth increase.

To demonstrate that these results are actually due to nonlinear effects in Al_2O_3 and not due to nonlinear effects in the fibers and adjacent components after the chip, the output fiber was defocussed (moved away from the chip) in steps given a certain on-chip power. This creates a situation with constant power on chip and varyingly decreasing power in the fiber (components) after the chip. Figure 2.24 shows the resulting spectra. The power was decreased by 4, 7, 10 and 13 dB. Aside from the expected downward shift, the shape from the spectra remains predomi-

nantly unchanged. If any significant nonlinear effects were taking place in the fibers, a change in spectrum would be expected. As this is not the case, we conclude that the nonlinear broadening of the light was indeed due to the Al_2O_3 chip.

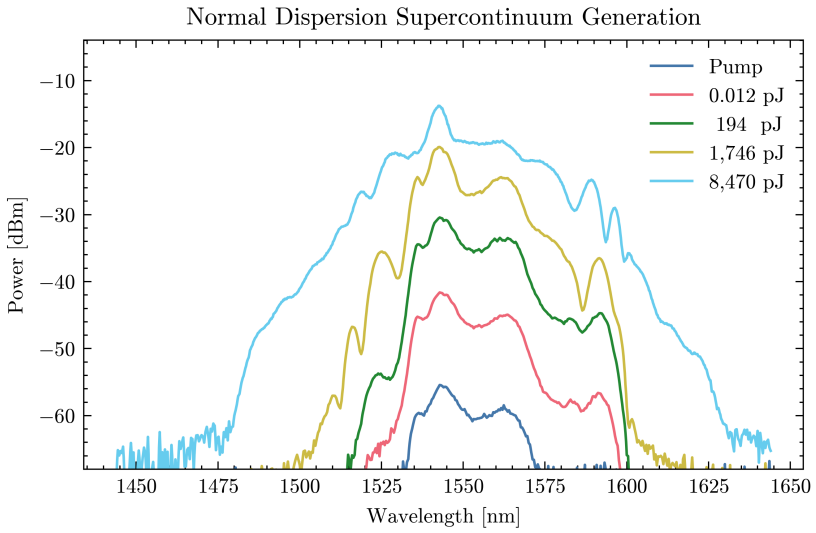

Figure 2.23: Recorded spectra of broadening with increasing pulse energy on chip.

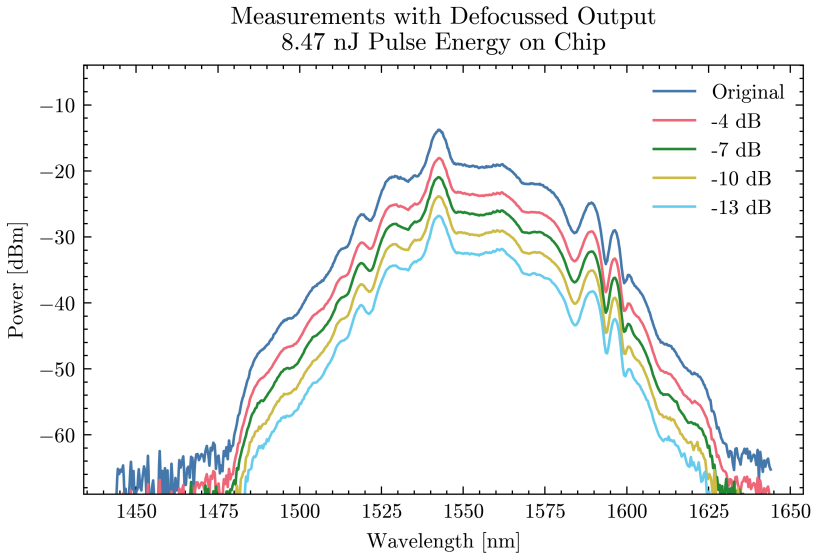

Figure 2.24: Recorded spectra of broadening with constant power on chip, but decreasing output power through defocussing.

Damage threshold

Although no failure of the waveguide due to the high-power pulses has been found during experiments, we can still conclude a lower-limit of the pulsed laser damage threshold of Al_2O_3. The value is expressed in the maximum determined fluence F in the waveguide, where:

$$F = \frac{E_p}{A_{\text{eff}}}. \tag{2.14}$$

Here E_p is the pulse energy and A_{eff} the effective mode area of the pump. The A_{eff} of the waveguide was found to be 2.847 μm^2 through simulations with Lumerical MODE. Combined with the maximum pulse energy of 8.47 nJ, this gives a minimum power handling capability of 0.298 J/cm^2, with a pulse width of 164 fs at a wavelength of 1544 nm.

2.6 Discussion

This chapter started with a general theoretical overview to introduce the concept of SCG in PICs. Although these models have been refined and successfully used for many years, SCG is still a hugely complex process and many approximations and simplifications were used in the design and simulations.

The design of the PIC focused on dispersive waves and SCG reaching into the UV, with one of its primary design choices being the 1064 nm light source. Although the addition of extra edge couplers for 1550 nm provided some flexibility and proved very useful as a backup in this case, the chips are still limited in terms of their optimally compatible pump wavelengths, with 1064 nm being the only one in the anomalous dispersion regime. In hindsight, it might have been beneficial to include structures to allow for more possible wavelengths for future research outside that of my own. That being said, the use of free-space lasers offers more flexibility for coupling, making other lasers not completely impractical to use, and the structures were shown to work well at 1550 nm.

Simulations have shown significant potential for SCG and dispersive waves into the UV. A large point of discussion is that the simulations did not take into account the material losses, which might especially influence the lower wavelengths where losses tend to be higher. Additionally, a blue shift is observed in the dispersive waves locations, compared to the predicted wavelength due to phase matching. The estimation is still in the correct order of magnitude and thus remains functional for approximate design. This deviations suggests more complex effects are at play. More accurate predictions would require a more elaborate approximation of the phase matching or possibly a set of experimental results which can be fitted to a predictive model. Future work could benefit from classifying the effects at multiple waveguide widths and creating a relation for experimentally determined dispersive waves for each width, which would function as a valuable reference to future dispersion engineering.

The chip fabrication was successful and inspected using a microscope. In simulations and design, the dimensions and value for properties like n_{eff}, thickness and width are taken as constant and do not take into account any variance in the wafer. Variances in fabrication are inevitable, and could lead to significant deviations between experiments and simulation, thus, there is likely a benefit from high-resolution characterisations of the dimensions (for example using SEM imaging) for future research.

Of course, the largest influence on the experiments was the use of the 1550 nm laser instead of the 1064 nm laser. This prevented validation of the simulated anomalous dispersion results. It did, however, show that the structures on the chip are guiding properly and it allowed for both the demonstration of some nonlinear effects in Al_2O_3 based waveguides as well as for the determination of a lower limit on the damage threshold.

In summary, this work has demonstrated the potential for using Al_2O_3 for SCG and provided physical PICs for future research. Future work can focus on characterizing the design wavelength and validating simulation results with experiments to provide a more complete understanding of the capabilities and limitations of Al_2O_3 for SCG. All working together towards being able to generate into the UV spectrum in Al_2O_3.

Nonlinear Refractive Index in Al_2O_3 Waveguides through Four-Wave Mixing

***Abstract*—Nonlinear photonics in integrated photonic circuits (PICs) is a revolutionary technology, but still challenged in extending their range into the UV range. In this work the nonlinear properties of Al_2O_3 are explored, a material with broad transparency from 170 nm to the IR. Though analysis of four-wave mixing in micro-ring resonators with an intrinsic Q of 2.2 million, we experimentally determined the nonlinear refractive index of Al_2O_3 to be $n_2 = (2.6 \pm 0.17) \cdot 10^{-20}$, which is consistent with bulk measurements. We also determined a power handling capability of at least 21 W in the C-band, making Al_2O_3 a valuable material in both high- and low-power photonics.**

***Index Terms*—Aluminium oxide, nonlinear photonics, four-wave mixing, integrated photonics**

I. Introduction

Aluminum-based materials are emerging as very promising in the photonic space due to their broad transparency window, extending from 170 nm in the UV, into well into the IR [1]. While AlN is known for a relatively high nonlinear index, comparable to that of SiN, Al_2O_3 is less explored. Research on bulk materials indicates a nonlinear index for Al_2O_3 comparable to that of SiO2 [2]–[5], which is about an order of magnitude smaller than SiN [6]. This could position Al_2O_3 as a great linear companion to AlN in a multi-material platform or as a material that can selectively exhibit nonlinear performance in high-power-enhancing structures like micro-ring resonators (MRR) with high Q factors.

In this work, we determine the nonlinear index n_2 of Al_2O_3 through an analysis of the four-wave mixing performance in high-Q, low-loss MRRs. Using ring characterization and measured conversion efficiencies, we report what is, to the best of our knowledge, the first nonlinear index of polycrystalline Al_2O_3 in a waveguide.

II. Fabrication

The Al_2O_3 structures were defined on a 447 nm thick film using electron-beam lithography (EBL). A negative resist of 1000 µC/cm^2 was patterned and reactive ion-etching (RIE) was used to define the waveguides and rings. The film deposition was performed using reactive magnetron sputtering on a 10 cm diameter silicon wafer with an eight µm thermal oxide layer. After this an eight µm thick SiO_2 cladding is deposited using Plasma-enhanced chemical vapor deposition (PECVD). Deposition and lithography were performed in the MESA+ Nanolab following procedures outlined in [7], [8].

Figure 1 shows a schematic of the micro-ring resonator design. The waveguides have a width of 1.5 µm with a sidewall of approximately 70°. The gap distance between the bus waveguide and the ring is 1.8 µm, making the ring slightly under-coupled. The radius of the ring is 250 µm. Figure 2 shows a mode-analyse made using Lumerical MODE solver. The waveguides exhibit an effective mode area A_{eff} of 1.892 at a 1550 nm wavelength µm^2 for the fundamental TE mode.

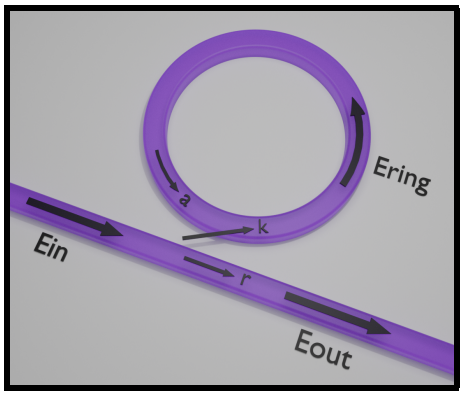

Fig. 1. A schematic of the micro-ring resonator with the cross-coupling coefficient k, the self-coupling coefficient r, and the round trip attenuation a.

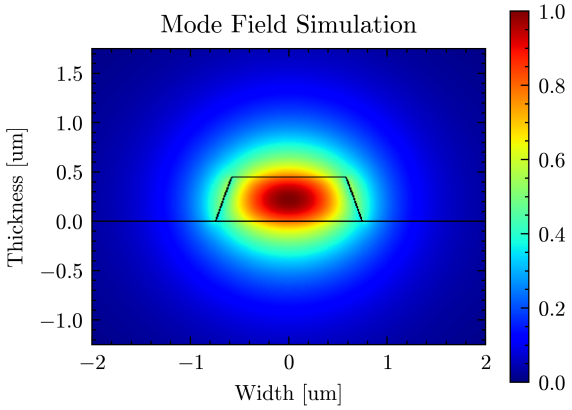

Fig. 2. E-intensity modal field. Made using Lumerical software.

III. Characterisation

To characterize the performance of the ring, a Superluminescent Diode (SLD) was used to illuminate the rings with a broadband signal, with a fiber polarizing beam splitter (PBS) to filter the input to isolate the TE polarization. The output power was recorded using a high-resolution Optical Spectrum Analyzer (OSA) (Finisar 1500S WaveAnalyser) from 1546 nm to 1554 nm with a resolution of 0.16 pm. After normalising the output with respect to the transmission, we applied a Lorentzian fit to the resonances (see Figure 3). From the full width half maximum (FWHM) and minimum transmissions of these fits the loaded quality

factor Q_l and the intrinsic quality factor Q_{int} [9], [10] can be calculated using:

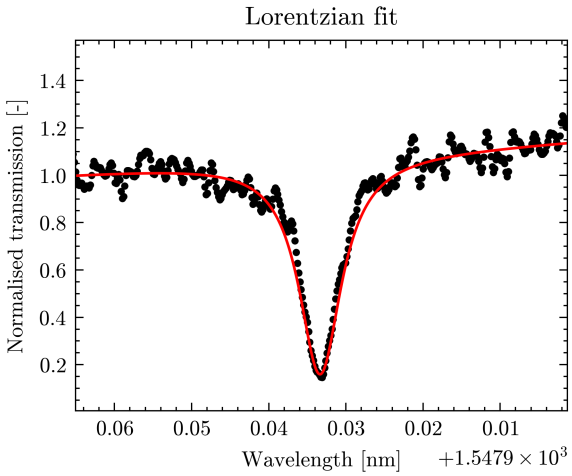

Fig. 3. Measured ring resonance with Lorentzian fit.

$$Q_l = \frac{\lambda_0}{\text{FWHM}} \tag{1}$$

$$Q_{int} = \frac{2Q_l}{1 - \sqrt{T_{min}}} \tag{2}$$

Where λ_0 is the central wavelength of a resonance. The Free Spectral Range (FSR) is the average distance between the resonant peaks. The group index n_g is determined using:

$$n_g = \frac{\lambda_0^2}{L \cdot \text{FSR}}, \tag{3}$$

The cross power coupling coefficients k^2 is expressed as: [11]

$$k^2 = \frac{(1 - \sqrt{T_{min}})\pi}{\text{FSR}} \cdot \text{FWHM}. \tag{4}$$

The self power coupling coefficient r^2 is equal to $1 - k^2$ assuming a lossless coupling section. The round trip loss a can be determined from the general equation for transmission of a micro-ring resonator [9], [10]:

$$T = \frac{r^2 - 2ra\cos(\frac{2\pi\Delta\lambda}{\text{FSR}}) + a^2}{1 - 2ra\cos(\frac{2\pi\Delta\lambda}{\text{FSR}}) + (ra)^2}, \tag{5}$$

where $\Delta\lambda$ is the detuning with respect to the center wavelength. Note that when $\Delta\lambda = 0$, $T = T_{min}$. The instrinsic loss α can be found using $a = \exp(-\alpha L/2)$. This intrinsic loss is used to determine the effective length L' of the ring resonator:

$$L' = \frac{1 - e^{-\alpha L}}{\alpha}. \tag{6}$$

Following measurements and the above equations, the intrinsic loss of the material was determined to be $\alpha = 0.37\text{dBcm}^{-1}$. The average intrinsic Q-factor was found to be $Q_{int} = 2,210,454$ and the average loaded Q-factor was $Q_l = 895,580$.

IV. Methodology Four-Wave Mixing

Two tunable lasers, in conjunction with two high-power erbium-doped fiber amplifiers (EDFAs), were used to excite the rings. The lasers were combined in a 50:50 fiber coupler and TE polarized through a PBS controlled with polarization controllers, schematically depicted in Figure 4. The output spectra were measured with a high resolution OSA (Finisar 1500S WaveAnalyser [12]). The signal laser power was set to 20 dBm and the pump laser power was gradually increased from 30 dBm until 38 dBm. The lasers were tuned to be in resonance with the MRR by maximizing their extinction ratios and the polarization was tuned to TE by minimizing the rejected power form the PBS.

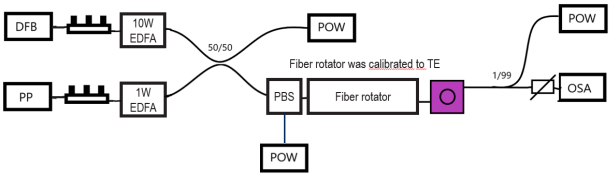

Fig. 4. Schematic overview of measurement setup.

For FWM, the conversion efficiency η is defined as the ratio between the off-resonance signal power and the highest generated side band, called the converter. It follows the following relation [13]:

$$\eta = \frac{P_c}{P_{s,in}} = |L'\gamma P_p|^2 \cdot PE_p^2 PE_s PE_c, \tag{7}$$

where the PE terms denote the power enhancement factors for the pump, signal, and converter, respectively. These power enhancement factors follow the general equation [9]:

$$\text{PE} = \frac{k}{1 - 2ra\cos\left(\frac{2\pi\Delta\lambda}{\text{FSR}}\right) + (ra)^2}. \tag{8}$$

The power enhancement is significantly dependant on the detuning, which in many cases the detuning should not be assumed negligible. Especially at higher powers due to thermal instability. Detuning can be determined using the measured transmission T and the properties of the rings. Solving Equation 5 for the detuning gives:

$$\Delta\lambda = \frac{a^2 r^2 T - a^2 - r^2 + T}{4\pi \cdot ra(T-1)} \cdot \text{FSR} \tag{9}$$

Note that the detuning of the converter is calculated using $2\Delta\lambda_p = \Delta\lambda_s$ with the assumption of a constant FSR between the resonances. The calculation for PE is repeated for the pump, signal, and converter for each measurement. With that the conversion efficiency from Equation 7 can be normalised with respect to the power enhancement:

$$\eta_{norm} = \frac{\eta}{PE_p^2 PE_s PE_c} = |L'\gamma P_p|^2. \tag{10}$$

Which can be rewritten in dB units for γ as

$$\gamma = \frac{1}{L'} \exp\left(\frac{\eta_{norm,dB}}{P_{p,dBm} \cdot 20} + 3\right), \tag{11}$$

where $\frac{\eta_{norm,dB}}{P_{p,dBm}}$ is the slope of normalised conversion efficiency measurements taken at multiple powers in a dB plot. From this the nonlinear index can be extracted using:

$$n_2 = \frac{\gamma A_{\text{eff}} \lambda}{2\pi}, \tag{12}$$

V. Experimental Results

Figure 5 shown an example spectrum with an overlay of both in- and out-resonance tuning of the input lasers. We can see clear sidebands with a spacing equal to the FSR when in-resonance, indicating the presence of four-wave mixing. No sidebands outside of resonance is a strong indication that the power enhancement inside of the MRR is responsible for the nonlinear effects and not the (external) fiber or components.

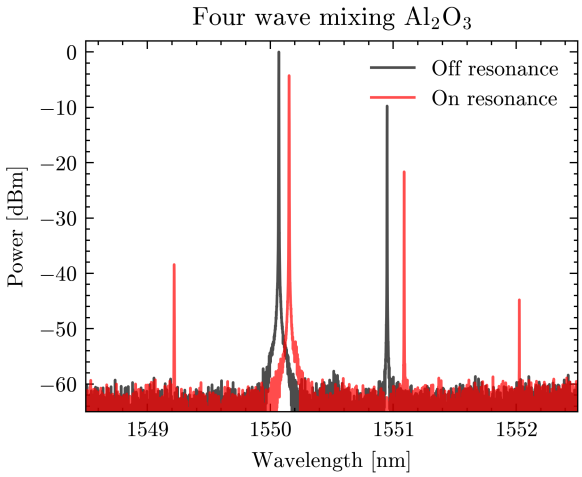

Fig. 5. Superimposed output of spectra with lasers on- and off-resonance. FWM side bands are clearly only visible with the lasers on-resonance.

The average power enhancement over all measurements was 48.7, resulting in an averaged total enhancement $PE_p^2 PE_s PE_c \approx 5.2 \cdot 10^6$. The pump power was successfully increased until 38 dBm, above which which the critical damage threshold for the facets of the photonic chip was found between the bus waveguide powers of 437mW and 580mW. Using the average power enhancement of 48.7 we estimate the minimum power handling of the waveguides to be over 21 W for constant wave (CW) lasers in the C-band.

Figure 6 shows the measured normalised efficiency against the bus power in the chip. Note how the slope is nearly two which is expected for FWM in a dB plot, due to the quadratic dependence on the bus power, see Equation 7. From this data a γ of $5.6 \cdot 10^{-2}$ $\text{W}^{-1}\text{m}^{-1}$ was extracted, which resulted in a nonlinear index of $n_2 = (2.6 \pm 0.17) \cdot 10^{-20}$ m^2/W.

This value falls nicely in the range of nonlinear index measurements done in bulk materials, see Figure 7 for a comparison with values from [refs]. For a comparison to other photonic waveguide materials, see Table I.

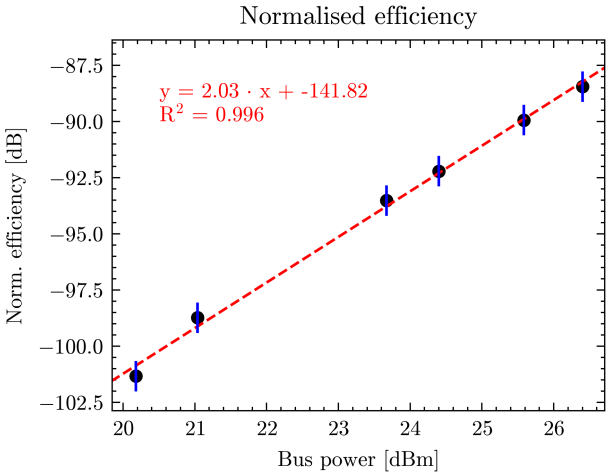

Fig. 6. Measured normalised efficiency. Equation shows the linear fit through the data. From the fit γ is extracted, with an A_{eff} of 1.892

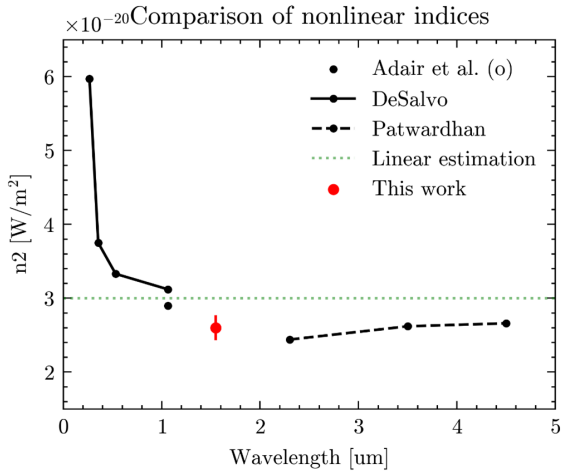

Fig. 7. Comparison with difference measured value for the nonlinear refractive index in bulk Al_2O_3. Values from [2]–[4], collected in [14].

VI. Conclusion

In this study, we demonstrated clear four-wave mixing in a material not known for high non-linearity. The waveguide micro-ring resonator exhibited a power enhancement of 48.7 with an intrinsic Q factor of 895,580. We achieved a maximum conversion efficiency in the ring of -21.46dB, corresponding to an effective conversion efficiency of -88.45dB, resulting in a nonlinear index of $n2 = (2.6 \pm 0.17) \cdot 10^{-20}$ m^2/W. This demonstrates that indeed Al_2O_3 does not easily exhibit nonlinear effects, showing a similar nonlinear index to SiO_2 and being about a approximately an order of magnitude lower than AlN and SiN. We've also shown a power handling capability of at least 21 W in the C-band. To the best of our knowledge, this n_2 value is the first experimentally determined nonlinear index value for polycrystalline Al_2O_3 in a waveguide structure.

References

[1] N. Li, C. P. Ho, S. Zhu, Y. H. Fu, Y. Zhu, and L. Y. T. Lee, "Aluminium nitride integrated photonics: a review," *Nanophotonics*, vol. 10, pp. 2347–2387, July 2021.

[2] R. DeSalvo, A. Said, D. Hagan, E. Van Stryland, and M. Sheik-Bahae, "Infrared to ultraviolet measurements of two-photon absorption and n/sub 2/ in wide bandgap solids," *IEEE Journal of Quantum*

TABLE I
COMPARISON OF NONLINEAR INDICES

Material	n_2 (m^2/W) @ 1550nm
Al_2O_3	$\mathbf{2.6 \cdot 10^{-20}}$
SiO_2 [5]	$2.42 \cdot 10^{-20}$
AlN [1]	$2.3 \cdot 10^{-19}$
SiN [6]	$2.4 \cdot 10^{-19}$

Electronics, vol. 32, pp. 1324–1333, Aug. 1996. Conference Name: IEEE Journal of Quantum Electronics.

[3] R. Adair, L. L. Chase, and S. A. Payne, "Nonlinear refractive index of optical crystals," *Physical Review B*, vol. 39, pp. 3337–3350, Feb. 1989. Publisher: American Physical Society.

[4] G. N. Patwardhan, J. S. Ginsberg, C. Y. Chen, M. M. Jadidi, and A. L. Gaeta, "Nonlinear refractive index of solids in mid-infrared," *Optics Letters*, vol. 46, pp. 1824–1827, Apr. 2021. Publisher: Optica Publishing Group.

[5] S. R. Flom, G. Beadie, S. S. Bayya, B. Shaw, and J. M. Auxier, "Ultrafast Z-scan measurements of nonlinear optical constants of window materials at 772, 1030, and 1550nm," *Applied Optics*, vol. 54, pp. F123–F128, Nov. 2015. Publisher: Optica Publishing Group.

[6] K. Ikeda, R. E. Saperstein, N. Alic, and Y. Fainman, "Thermal and Kerr nonlinear properties of plasma-deposited silicon nitride/silicon dioxide waveguides," *Optics Express*, vol. 16, pp. 12987–12994, Aug. 2008. Publisher: Optica Publishing Group.

[7] C. I. v. Emmerik, W. A. P. M. Hendriks, M. M. Stok, M. d. Goede, L. Chang, M. Dijkstra, F. Segerink, D. Post, E. G. Keim, M. J. Dikkers, and S. M. García-Blanco, "Relative oxidation state of the target as guideline for depositing optical quality RF reactive magnetron sputtered Al_2O_3 layers," *Optical Materials Express*, vol. 10, pp. 1451–1462, June 2020. Publisher: Optica Publishing Group.

[8] D. B. Bonneville, C. E. Osornio-Martinez, M. Dijkstra, and S. M. García-Blanco, "High on-chip gain spiral Al_2O_3:Er^{3+} waveguide amplifiers," *Optics Express*, vol. 32, pp. 15527–15536, Apr. 2024. Publisher: Optica Publishing Group.

[9] *Optical Microresonators*, vol. 138 of *Optical Sciences*. New York, NY: Springer, 2008.

[10] W. Bogaerts, P. De Heyn, T. Van Vaerenbergh, K. De Vos, S. Kumar Selvaraja, T. Claes, P. Dumon, P. Bienstman, D. Van Thourhout, and R. Baets, "Silicon microring resonators," *Laser & Photonics Reviews*, vol. 6, pp. 47–73, Jan. 2012.

[11] J. Hong, K. Rokumyo, J. Mao, A. Bannaron, H. Sato, and S. Yokoyama, "Efficient four-wave mixing wavelength conversion in a hybrid silicon slot and polymer microring resonator," *Optics Express*, vol. 30, pp. 45499–45507, Dec. 2022. Publisher: Optica Publishing Group.

[12] "WaveAnalyzer High-Resolution Optical Spectral Analysis,"

[13] P. P. Absil, J. V. Hryniewicz, B. E. Little, P. S. Cho, R. A. Wilson, L. G. Joneckis, and P.-T. Ho, "Wavelength conversion in GaAs micro-ring resonators," *Optics Letters*, vol. 25, pp. 554–556, Apr. 2000. Publisher: Optica Publishing Group.

[14] M. N. Polyanskiy, "Refractiveindex.info database of optical constants," *Scientific Data*, vol. 11, p. 94, Jan. 2024. Publisher: Nature Publishing Group.

Chapter 4

Conclusion

In this thesis, the potential of Al_2O_3 for supercontinuum generation (SCG) and its nonlinear refractive index has been studied. The work was divided into two main research questions: demonstrating SCG in Al_2O_3 integrated waveguides and determining the nonlinear refractive index of polycrystalline Al_2O_3 waveguides.

The first research question focused on demonstrating SCG in Al_2O_3 waveguides:

"*Is it possible to demonstrate supercontinuum generation in Al2O3 based integrated waveguides?*"

With the sub-question:
What is the damage threshold of Al_2O_3 for ultra-fast pulsed lasers?

The theoretical groundwork and design choices were centered on achieving SCG into the UV, with a primary design wavelength of 1064 nm. Despite challenges like the unavailability of the intended laser source, the backup 1550 nm laser still allowed experiments. The simulations showed potential for SCG and showed dispersive waves extending into the UV spectrum. Although the experiments were limited to normal dispersion regimes, they confirmed nonlinear effects in Al_2O_3 and a lower-limit on the **damage threshold of 0.298 J/cm^2**, with a pulse width of 164 fs at a wavelength of 1544 nm. This together makes it very likely that SCG can be demonstrated in Al_2O_3 waveguides, even though it could not be achieved in this study.

The second research question aimed to determine material properties of Al_2O_3 through four-wave mixing (FWM) in micro-ring resonators (MRRs), more specifically:

What is the nonlinear refractive index of polycrystalline Al_2O_3 based integrated waveguides?

With the sub-question:
What is the damage threshold of Al_2O_3 for continuous-wave lasers?

Using the characterised high-Q MMRs and through the analysis of measurements of the FWM process, we determined the **nonlinear refractive index $\mathbf{n_2}$ to b**e $(\mathbf{2.6 \pm 0.17})$ $\mathbf{\cdot 10^{-20}}$ **m²/W**. This value is consistent with previously reported values for bulk Al_2O_3 and linear approximations, making a argument for the relative accuracy of the value for PICs. Additionally, the power handling capability of the waveguides was demonstrated to be over **21 W in the C-band**, indicating their suitability for high-power photonic applications.

Overall, this thesis has demonstrated that Al_2O_3 is a promising material for SCG, especially for applications requiring UV transparency. Its relatively low nonlinear refractive index is compensated by its high power handling and transparency into the UV. My hope is that this work will serve as the foundation for numerous future experiments, possibly including the validation of the design of these PICs through the intended laser source, to further explore the potential of Al_2O_3 for SCG into the UV and other Al_2O_3 based nonlinear applications on chip.

Bibliography

[1] K. Asakawa, Y. Sugimoto, and S. Nakamura, "Silicon photonics for telecom and data-com applications," *Opto-Electronic Advances*, vol. 3, pp. 200011–26, Oct. 2020. Publisher: Opto-Electronic Advances.

[2] W. Hendriks, M. Dijkstra, J. Korterik, and S. G. Blanco, "Al2O3 referenced microring resonators for the detection of interleukin-6," in *2021 IEEE 17th International Conference on Group IV Photonics (GFP)*, pp. 1–2, Dec. 2021. ISSN: 1949-209X.

[3] N. L. Kazanskiy, S. N. Khonina, and M. A. Butt, "Advancement in Silicon Integrated Photonics Technologies for Sensing Applications in Near-Infrared and Mid-Infrared Region: A Review," *Photonics*, vol. 9, p. 331, May 2022. Number: 5 Publisher: Multidisciplinary Digital Publishing Institute.

[4] M. Krainak, M. Stephen, E. Troupaki, S. Tedder, B. Reyna, J. Klamkin, H. Zhao, B. Song, J. Fridlander, M. Tran, J. E. Bowers, K. Bergman, M. Lipson, A. Rizzo, I. Datta, N. Abrams, S. Mookherjea, S.-T. Ho, Q. Bei, Y. Huang, Y. Tu, B. Moslehi, J. Harris, A. Matsko, A. Savchenkov, G. Liu, R. Proietti, S. J. B. Yoo, L. Johansson, C. Dorrer, F. R. Arteaga-Sierra, J. Qiao, S. Gong, T. Gu, O. J. O. Iii, X. Ni, Y. Ding, Y. Duan, H. Dalir, R. T. Chen, V. J. Sorger, and T. Komljenovic, "Integrated photonics for NASA applications," in *Components and Packaging for Laser Systems V*, vol. 10899, pp. 75–94, SPIE, Mar. 2019.

[5] K. M. Yoo, J. Midkiff, A. Rostamian, C.-j. Chung, H. Dalir, and R. T. Chen, "InGaAs Membrane Waveguide: A Promising Platform for Monolithic Integrated Mid-Infrared Optical Gas Sensor," *ACS Sensors*, vol. 5, pp. 861–869, Mar. 2020. Publisher: American Chemical Society.

[6] D. B. Bonneville, C. E. Osornio-Martinez, M. Dijkstra, and S. M. García-Blanco, "High on-chip gain spiral Al2O3:Er3+ waveguide amplifiers," *Optics express*, vol. 32, pp. 15527–15536, Apr. 2024. Publisher: The Optical Society.

[7] Y. Wang, J. A. Holguín-Lerma, M. Vezzoli, Y. Guo, and H. X. Tang, "Photonic-circuit-integrated titanium:sapphire laser," *Nature Photonics*, vol. 17, pp. 338–345, Apr. 2023. Publisher: Nature Publishing Group.

[8] E. Pelucchi, G. Fagas, I. Aharonovich, D. Englund, E. Figueroa, Q. Gong, H. Hannes, J. Liu, C.-Y. Lu, N. Matsuda, J.-W. Pan, F. Schreck, F. Sciarrino, C. Silberhorn, J. Wang, and K. D. Jöns, "The potential and global outlook of integrated photonics for quantum technologies," *Nature Reviews Physics*, vol. 4, pp. 194–208, Mar. 2022. Publisher: Nature Publishing Group.

[9] C.-S. Brès, A. D. Torre, D. Grassani, V. Brasch, C. Grillet, and C. Monat, "Supercontinuum in integrated photonics: generation, applications, challenges, and perspectives," *Nanophotonics*, vol. 12, pp. 1199–1244, Apr. 2023. Publisher: De Gruyter.

[10] C. Lafforgue, M. Montesinos-Ballester, T.-T.-D. Dinh, X. L. Roux, E. Cassan, D. Marris-Morini, C. Alonso-Ramos, and L. Vivien, "Supercontinuum generation in silicon photonics platforms," *Photonics Research*, vol. 10, pp. A43–A56, Mar. 2022. Publisher: Optica Publishing Group.

[11] C. Lin and R. H. Stolen, "New nanosecond continuum for excited-state spectroscopy," *Applied Physics Letters*, vol. 28, pp. 216–218, Feb. 1976.

[12] D. J. Blumenthal, R. Heideman, D. Geuzebroek, A. Leinse, and C. Roeloffzen, "Silicon Nitride in Silicon Photonics," *Proceedings of the IEEE*, vol. 106, pp. 2209–2231, Dec. 2018. Conference Name: Proceedings of the IEEE.

[13] X. Guo, X. Ji, B. Yao, T. Tan, A. Chu, O. Westreich, A. Dutt, C. Wong, and Y. Su, "Ultra-wideband integrated photonic devices on silicon platform: from visible to mid-IR," *Nanophotonics*, vol. 12, Jan. 2023.

[14] W. a. P. M. Hendriks, M. Dijkstra, C. I. v. Emmerik, I. Hegeman, and S. M. G. Blanco, "High refractive index low-loss aluminium oxide waveguides," June 2020.

[15] M. N. Polyanskiy, "Refractiveindex.info database of optical constants," *Scientific Data*, vol. 11, p. 94, Jan. 2024. Publisher: Nature Publishing Group.

[16] G. Agrawal, "Chapter 13 - Supercontinuum Generation," in *Nonlinear Fiber Optics (Fifth Edition)* (G. Agrawal, ed.), Optics and Photonics, pp. 553–612, Boston: Academic Press, Jan. 2013.

[17] D. R. Paschotta, "supercontinuum generation."

[18] "Aluvia Photonics."

[19] G. P. Agrawal, "Chapter 6 - Polarization Effects," in *Nonlinear Fiber Optics (Fifth Edition)* (G. Agrawal, ed.), Optics and Photonics, pp. 193–244, Boston: Academic Press, Jan. 2013.

[20] D. R. Paschotta, "Kerr effect."

[21] R. W. Boyd, "Chapter 1 - The Nonlinear Optical Susceptibility," in *Nonlinear Optics (Fourth Edition)* (R. W. Boyd, ed.), pp. 1–64, Academic Press, Jan. 2020.

[22] G. Agrawal, "Chapter 3 - Group-Velocity Dispersion," in *Nonlinear Fiber Optics (Fifth Edition)* (G. Agrawal, ed.), Optics and Photonics, pp. 57–85, Boston: Academic Press, Jan. 2013.

[23] D. R. Paschotta, "group velocity dispersion."

[24] R. W. Boyd, "Chapter 7 - Processes Resulting from the Intensity-Dependent Refractive Index," in *Nonlinear Optics (Fourth Edition)* (R. W. Boyd, ed.), pp. 321–380, Academic Press, Jan. 2020.

[25] J. Epping, *Dispersion engineering silicon nitride waveguides for broadband nonlinear frequency conversion*. PhD, University of Twente, Enschede, The Netherlands, Sept. 2015. ISBN: 9789036539395.

[26] R. W. Boyd, "Chapter 13 - Ultrafast and Intense-Field Nonlinear Optics," in *Nonlinear Optics (Fourth Edition)* (R. W. Boyd, ed.), pp. 541–568, Academic Press, Jan. 2020.

[27] D. R. Paschotta, "Raman scattering."

[28] D. R. Paschotta, "self-steepening."

[29] A. A. Voronin and A. M. Zheltikov, "Soliton self-frequency shift decelerated by self-steepening," *Optics Letters*, vol. 33, pp. 1723–1725, Aug. 2008. Publisher: Optica Publishing Group.

[30] G. Agrawal, "Chapter 4 - Self-Phase Modulation," in *Nonlinear Fiber Optics (Fifth Edition)* (G. Agrawal, ed.), Optics and Photonics, pp. 87–128, Boston: Academic Press, Jan. 2013.

[31] G. Agrawal, “Chapter 7 - Cross-Phase Modulation,” in *Nonlinear Fiber Optics (Fifth Edition)* (G. Agrawal, ed.), Optics and Photonics, pp. 245–293, Boston: Academic Press, Jan. 2013.

[32] G. Agrawal, “Chapter 10 - Four-Wave Mixing,” in *Nonlinear Fiber Optics (Fifth Edition)* (G. Agrawal, ed.), Optics and Photonics, pp. 397–456, Boston: Academic Press, Jan. 2013.

[33] D. R. Paschotta, “four-wave mixing.”

[34] O. Krarup, *Enhancement of Fiber Optical Environmental Sensor Performance Via All-Optical Signal Processing*. PhD thesis, Université d’Ottawa / University of Ottawa, Mar. 2024.

[35] M. Buchanan, “Wave of translation,” *Nature Physics*, vol. 2, pp. 575–575, Sept. 2006. Publisher: Nature Publishing Group.

[36] “Optical Soliton - an overview | ScienceDirect Topics.”

[37] A. Adamski, “Soliton phenomena in the process of the functioning of the heart,” *Journal of Cardiology and Cardiovascular Medicine*, vol. 8, pp. 021–028, Mar. 2023.

[38] S. Wang, X.-y. Tang, and S.-Y. Lou, “Soliton fission and fusion: Burgers equation and Sharma–Tasso–Olver equation,” *Chaos, Solitons & Fractals*, vol. 21, pp. 231–239, July 2004.

[39] D. R. Paschotta, “higher-order solitons.”

[40] G. P. Agrawal, “Chapter 5 - Optical Solitons,” in *Nonlinear Fiber Optics (Fifth Edition)* (G. Agrawal, ed.), Optics and Photonics, pp. 129–191, Boston: Academic Press, Jan. 2013.

[41] J. M. Dudley, G. Genty, and S. Coen, “Supercontinuum generation in photonic crystal fiber,” *Reviews of Modern Physics*, vol. 78, pp. 1135–1184, Oct. 2006. Publisher: American Physical Society.

[42] F. Vogelbacher, S. Nevlacsil, M. Sagmeister, J. Kraft, K. Unterrainer, and R. Hainberger, “Analysis of silicon nitride partial Euler waveguide bends,” *Optics Express*, vol. 27, pp. 31394–31406, Oct. 2019. Publisher: Optica Publishing Group.

[43] C. I. v. Emmerik, W. A. P. M. Hendriks, M. M. Stok, M. d. Goede, L. Chang, M. Dijkstra, F. Segerink, D. Post, E. G. Keim, M. J. Dikkers, and S. M. García-Blanco, “Relative oxidation state of the target as guideline for depositing optical quality RF reactive magnetron sputtered Al_2O_3 layers,” *Optical Materials Express*, vol. 10, pp. 1451–1462, June 2020. Publisher: Optica Publishing Group.

[44] D. B. Bonneville, C. E. Osornio-Martinez, M. Dijkstra, and S. M. García-Blanco, “High on-chip gain spiral Al_2O_3:Er^{3+} waveguide amplifiers,” *Optics Express*, vol. 32, pp. 15527–15536, Apr. 2024. Publisher: Optica Publishing Group.

[45] “Simulating supercontinua from mixed and cascaded nonlinearities | APL Photonics | AIP Publishing.”

[46] D. R. Austin, C. M. d. Sterke, B. J. Eggleton, and T. G. Brown, “Dispersive wave blue-shift in supercontinuum generation,” *Optics Express*, vol. 14, pp. 11997–12007, Dec. 2006. Publisher: Optica Publishing Group.

Appendix A

PIC Waveguide Information Sheet

Chip number	**Uncladded length** [cm]	**Total length** [cm]
0	*2.12*	*2.12*
1	1.42	*2.12*
2	0.72	*2.12*
3	0.00	*2.12*

All four chips are identical save for the uncladded region
First 36 waveguides have an edge coupler for 1064nm light
Last 36 waveguides have an edge coupler for 1550nm light
See information below

Values for 1064nm light

Number on chip	**Mode field** {edge coupler}	**Width** [um] {edge coupler}	**Width** [um] {waveguide}	**Thickness** [um]	**Length** [cm]	**TE Modes** {cladded}	**TE Modes** {uncladded}
1	*7.06*	*0.17*	0.60	*0.451*	*2.12*	Single	Poor confinement
2	*7.06*	*0.17*	0.70	*0.451*	*2.12*	Single	Single
3	*7.06*	*0.17*	0.80	*0.451*	*2.12*	Single	Single
4	*7.06*	*0.17*	0.90	*0.451*	*2.12*	Single	Single
5	*7.06*	*0.17*	1.00	*0.451*	*2.12*	Multi	Single
6	*7.06*	*0.17*	1.10	*0.451*	*2.12*	Multi	Single
7	*7.06*	*0.17*	1.20	*0.451*	*2.12*	Multi	Single
8	*7.06*	*0.17*	1.30	*0.451*	*2.12*	Multi	Single
9	*7.06*	*0.17*	1.40	*0.451*	*2.12*	Multi	Single
10	*7.06*	*0.17*	1.50	*0.451*	*2.12*	Multi	Single
11	*7.06*	*0.17*	1.60	*0.451*	*2.12*	Multi	Multi
12	*7.06*	*0.17*	1.82	*0.451*	*2.12*	Multi	Multi
13	*7.06*	*0.17*	2.04	*0.451*	*2.12*	Multi	Multi
14	*7.06*	*0.17*	2.26	*0.451*	*2.12*	Multi	Multi
15	*7.06*	*0.17*	2.48	*0.451*	*2.12*	Multi	Multi
16	*7.06*	*0.17*	2.70	*0.451*	*2.12*	Multi	Multi
17	*7.06*	*0.17*	2.92	*0.451*	*2.12*	Multi	Multi
18	*7.06*	*0.17*	3.14	*0.451*	*2.12*	Multi	Multi
19	*7.06*	*0.17*	3.36	*0.451*	*2.12*	Multi	Multi
20	*7.06*	*0.17*	3.58	*0.451*	*2.12*	Multi	Multi
21	*7.06*	*0.17*	3.80	*0.451*	*2.12*	Multi	Multi
22	*7.06*	*0.17*	4.02	*0.451*	*2.12*	Multi	Multi
23	*7.06*	*0.17*	4.24	*0.451*	*2.12*	Multi	Multi
24	*7.06*	*0.17*	4.46	*0.451*	*2.12*	Multi	Multi
25	*7.06*	*0.17*	4.68	*0.451*	*2.12*	Multi	Multi
26	*7.06*	*0.17*	4.90	*0.451*	*2.12*	Multi	Multi
27	*7.06*	*0.17*	5.12	*0.451*	*2.12*	Multi	Multi
28	*7.06*	*0.17*	5.34	*0.451*	*2.12*	Multi	Multi
29	*7.06*	*0.17*	5.56	*0.451*	*2.12*	Multi	Multi
30	*7.06*	*0.17*	5.78	*0.451*	*2.12*	Multi	Multi
31	*7.06*	*0.17*	6.00	*0.451*	*2.12*	Multi	Multi
32	*7.06*	*0.17*	7.00	*0.451*	*2.12*	Multi	Multi
33	*7.06*	*0.17*	8.00	*0.451*	*2.12*	Multi	Multi
34	*7.06*	*0.17*	9.00	*0.451*	*2.12*	Multi	Multi
35	*7.06*	*0.17*	10.00	*0.451*	*2.12*	Multi	Multi
36	*7.06*	*0.17*	11.00	*0.451*	*2.12*	Multi	Multi

Values for 1550nm light

Number on chip	**Mode field** {edge coupler}	**Width** [um] {edge coupler}	**Width** [um] {waveguide}	**Thickness** [um]	**Length** [cm]	**TE Modes** {cladded}	**TE Modes** {uncladded}
37	*6.58*	*0.38*	0.60	*0.451*	*2.12*	Single	Poor confinement
38	*6.58*	*0.38*	0.70	*0.451*	*2.12*	Single	Poor confinement
39	*6.58*	*0.38*	0.80	*0.451*	*2.12*	Single	Poor confinement
40	*6.58*	*0.38*	0.90	*0.451*	*2.12*	Single	Poor confinement
41	*6.58*	*0.38*	1.00	*0.451*	*2.12*	Single	Poor confinement
42	*6.58*	*0.38*	1.10	*0.451*	*2.12*	Single	Poor confinement
43	*6.58*	*0.38*	1.20	*0.451*	*2.12*	Single	Poor confinement
44	*6.58*	*0.38*	1.30	*0.451*	*2.12*	Single	Single
45	*6.58*	*0.38*	1.40	*0.451*	*2.12*	Single	Single
46	*6.58*	*0.38*	1.50	*0.451*	*2.12*	Single	Single
47	*6.58*	*0.38*	1.60	*0.451*	*2.12*	Single	Single
48	*6.58*	*0.38*	1.82	*0.451*	*2.12*	Multi	Single
49	*6.58*	*0.38*	2.04	*0.451*	*2.12*	Multi	Single
50	*6.58*	*0.38*	2.26	*0.451*	*2.12*	Multi	Single
51	*6.58*	*0.38*	2.48	*0.451*	*2.12*	Multi	Single
52	*6.58*	*0.38*	2.70	*0.451*	*2.12*	Multi	Single
53	*6.58*	*0.38*	2.92	*0.451*	*2.12*	Multi	Single
54	*6.58*	*0.38*	3.14	*0.451*	*2.12*	Multi	Multi
55	*6.58*	*0.38*	3.36	*0.451*	*2.12*	Multi	Multi
56	*6.58*	*0.38*	3.58	*0.451*	*2.12*	Multi	Multi
57	*6.58*	*0.38*	3.80	*0.451*	*2.12*	Multi	Multi
58	*6.58*	*0.38*	4.02	*0.451*	*2.12*	Multi	Multi
59	*6.58*	*0.38*	4.24	*0.451*	*2.12*	Multi	Multi
60	*6.58*	*0.38*	4.46	*0.451*	*2.12*	Multi	Multi
61	*6.58*	*0.38*	4.68	*0.451*	*2.12*	Multi	Multi
62	*6.58*	*0.38*	4.90	*0.451*	*2.12*	Multi	Multi
63	*6.58*	*0.38*	5.12	*0.451*	*2.12*	Multi	Multi
64	*6.58*	*0.38*	5.34	*0.451*	*2.12*	Multi	Multi
65	*6.58*	*0.38*	5.56	*0.451*	*2.12*	Multi	Multi
66	*6.58*	*0.38*	5.78	*0.451*	*2.12*	Multi	Multi
67	*6.58*	*0.38*	6.00	*0.451*	*2.12*	Multi	Multi
68	*6.58*	*0.38*	7.00	*0.451*	*2.12*	Multi	Multi
69	*6.58*	*0.38*	8.00	*0.451*	*2.12*	Multi	Multi
70	*6.58*	*0.38*	9.00	*0.451*	*2.12*	Multi	Multi
71	*6.58*	*0.38*	10.00	*0.451*	*2.12*	Multi	Multi
72	*6.58*	*0.38*	11.00	*0.451*	*2.12*	Multi	Multi

Appendix B

Quality Control Report: Toptica FF ULTRA 1560

01 General

Part No.:	FF ULTRA 1560 : 01083
Version:	1V0
Firmware version:	3.2.1
Production date:	28.04.2021

02 Components / IP Configuration

	laser head SN	**control unit SN**		
Arm 0	01083	null	/ -	/ -

03 Oscillator

	specification	measured
Repetition rate:	typ. 80 MHz	78.5 MHz

Optical emission spectrum:

RF - spectrum:

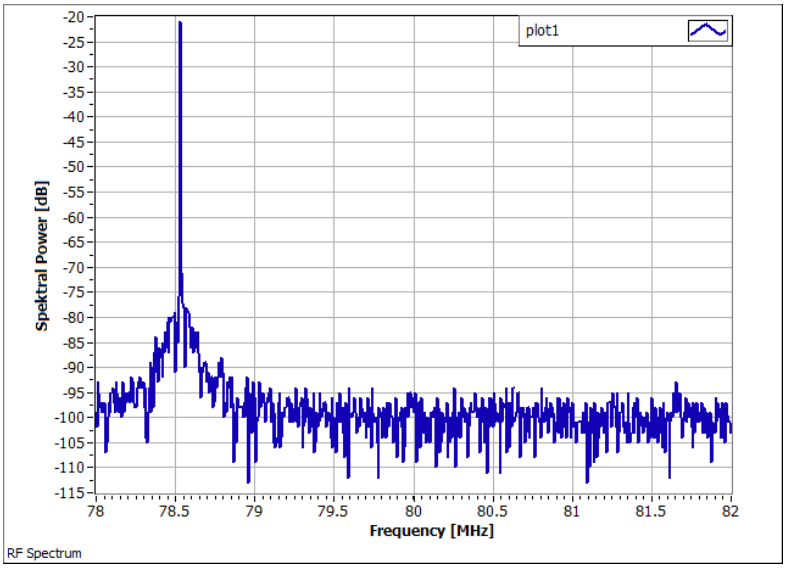

04 1560 nm - Output

	specification	measured
Central wavelength:	typ. 1560 nm	1544 nm
FWHM:	-	8 nm

Optical emission spectrum:

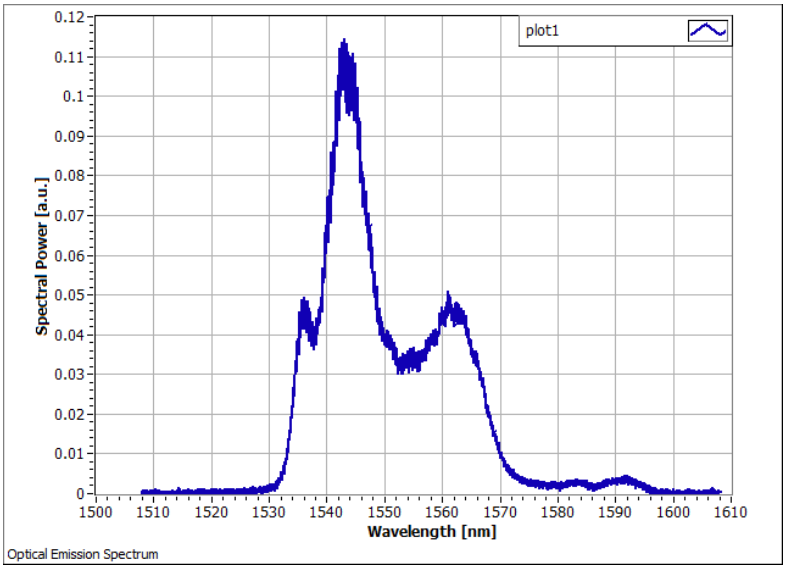

Intensity Autocorrelation:

	specification	measured
Pulse duration (assuming Sech2) :	< 200 fs	164.0 fs
Output power :	> 2 W	2.245 W

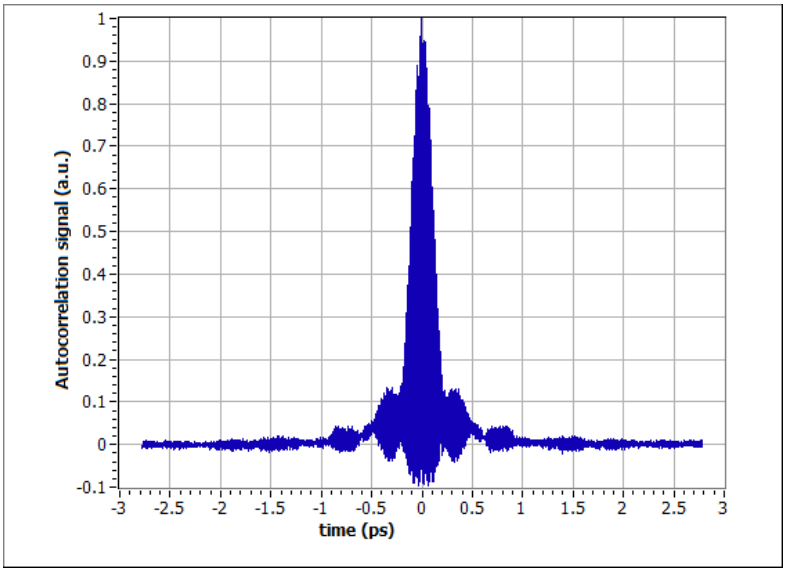

05 Optical Alignment

	specification	measured
X-Axis Beam Diameter (1/e²):	typ. 2 mm	1.38 mm
Y-Axis Beam Diameter (1/e²):	typ. 2 mm	1.41 mm
Ratio:	0.98	

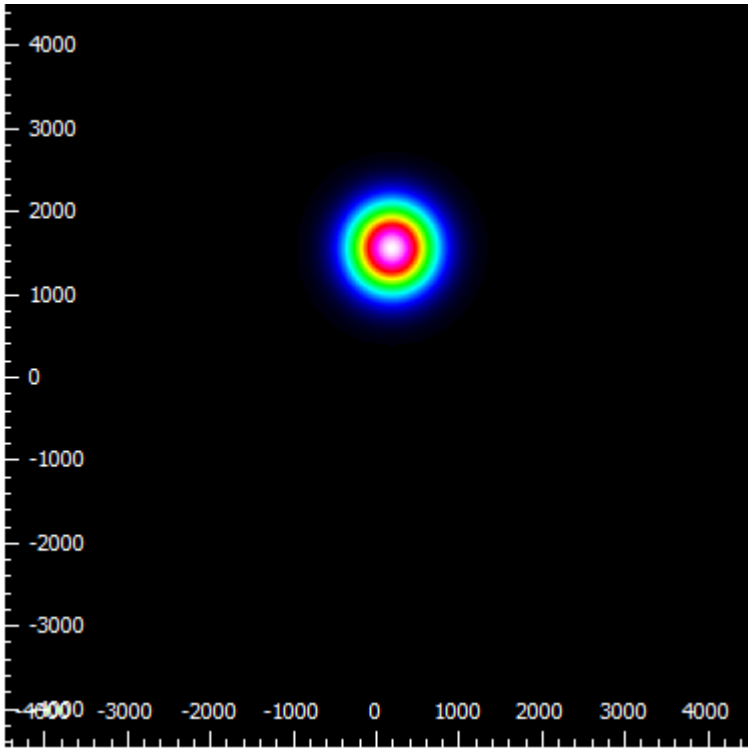

06 Quality Control

Production:	null	
Final Check:	Nguyen Thanh-Long	28.04.2021

01

Laser head and supply rack are connected by optical fibers during transportation

We recommend not to detach the fiber connection if not absolutely necessary!

02

It is recommended to lift the laser + supply rack by two persons in parallel!

03

Please make sure that the fiber is not suffering heavy pulls and bends when removing the system from the box.

04 Laser safety class 4 protection

After start-up of the laser (switching on power supply) the lase is in a locked status in order to prevent laser emission without manual confirmation.

In order to start the laser emission it is therfore necessary to manually confirm the laser start by either

- pressing laser emission button onse or
- switching the key switch "ON" -"OFF"-"ON"

After confirmation the laser emission can be startet either by pressing the laser emission button once again or by remote control interface

05 Optional AOM

Apply 5 Volt DC voltage to analog input for enabling laser emission output